Evaluation of aerosol optical depths and clear-sky radiative fluxes of the CERES Edition 4.1 SYN1deg data product

David W. Fillmore[1], David A. Rutan[2], Seiji Kato[3], Fred G. Rose[2],

and Thomas E. Caldwell[2]

[1]University Center for Atmospheric Research, Boulder, CO. 80307, USA

[2]SSAI, Hampton, VA, 23666, USA

[3]NASA Langley Research Center, Hampton, VA, 23666, USA

Submitted to

Atmospheric Chemistry and Physics

April 2021

Corresponding author address: David W Fillmore,
University Center for Atmospheric Research
P.O. Box 3000
Boulder, CO 80307
E-mail: david.w.fillmore@ucar.edu

Abstract

Aerosol optical depths (AOD) used for the Edition 4.1 Clouds and the Earth's Radiant Energy System (CERES) Synoptic (SYN1deg) are evaluated. AODs are derived from Moderate Resolution Imaging Spectroradiometer (MODIS) observations and assimilated by an aerosol transport model (MATCH). As a consequence, clear-sky AODs closely match with those derived from MODIS instruments. AODs under all-sky conditions are larger than AODs under clear-sky conditions, which is supported by ground-based AERONET observations. When all-sky MATCH AODs are compared with Modern-Era Retrospective Analysis for Research and Applications (MERRA2) AODs, MATCH AODs are generally larger than MERRA2 AODS especially over convective regions (e.g. Amazon, central Africa, and eastern Asia). The difference is largely caused by MODIS AODs used for assimilation. Including AODs with larger retrieval uncertainty makes AODs over the convective regions larger. When AODs are used for clear-sky irradiance computations and computed downward shortwave irradiances are compared with ground-based observations, the computed instantaneous irradiances are 1% to 2% larger than observed irradiances. The comparison of top-of-atmosphere clear-sky irradiances with those derived from CERES observations suggests that AODs used for surface radiation observation sites are larger by 0.01 to 0.03, which is within the uncertainty of instantaneous MODIS AODs. However, the comparison with AERONET AOD suggests AODs used for computations over desert sites are 0.08 larger. The cause of positive biases of downward shortwave irradiance and AODs for the desert sites is under investigation.

1. Introduction

Accurate estimates of the radiative effects of clouds and aerosols are essential for an understanding the radiative forcing to the Earth's climate system (Bauer and Menon, 2012, Boucher et al. 2013). In addition, through the reflection and absorption of solar radiation, and the absorption and emission of terrestrial thermal radiation, clouds and aerosols affect the radiative heating of both the atmosphere and the surface, which in turn governs the atmospheric circulation and the hydrological cycle (e.g. Stephens et al. 2020, L'Ecuyer et al. 2015). Under the Earth Observing System (EOS) program, the National Aeronautics and Space Administration (NASA) has placed into orbit a series of satellites devoted to long term observations of the climate state. Among these are Terra and Aqua, the flagship satellites of the EOS. Central to observation of climate evolution are Moderate Resolution Imaging Spectroradiometer (MODIS) and the Clouds and the Earth's Radiant Energy System (CERES) instrument pairs that fly on both the Terra (March 2000 - present) and the Aqua (July 2002 - present) platforms (Wielicki et al. 1996). Additional CERES instruments were launched (October 2011) upon the Suomi National Polar-orbiting Partnership (NPP) satellite along with the MODIS successor, the Visible Infrared Imager Radiometer Suite (VIIRS), and on the NOAA-20 satellite (November 2017). In addition to observations from these satellites, the CERES mission also integrates observations from the Geostationary Operational Environmental Satellites (GOES) (West and East), as well as other geostationary satellites around the globe, for full diurnal coverage of clouds and radiation.

72 The CERES instruments measure broadband radiances over the solar spectrum
73 (shortwave), the thermal infrared (longwave radiance is obtained from a total channel
74 minus the shortwave channel), and the near infrared atmospheric window, with frequent
75 on-board calibration. CERES measurements, in conjunction with MODIS information,
76 are used to infer broadband irradiances through empirical angular distribution models
77 (ADMs). Geosynchronous satellite imagery observes the diurnal cycle of clouds, which is
78 not fully sampled by the polar orbiting satellites upon which CERES and MODIS reside.
79 While top-of-atmosphere (TOA) irradiances are derived from broadband
80 radiances measured by CERES instruments (Loeb et al. 2005; Su et al. 2015), surface and
81 in atmosphere irradiances are computed with a radiative transfer model. Inputs used for
82 the computations include cloud properties derived from MODIS and geostationary
83 satellites, aerosol optical depth derived from MODIS radiances, and surface albedo
84 derived from MODIS and CERES observations (Rutan et al. 2009). Temperature and
85 humidity profiles are provided by a reanalysis product produced by the NASA Goddard
86 Modeling and Assimilation Office (GMAO).
87 Irradiances at the surface produced by the CERES team have been compared with
88 surface observations (Rutan et al. 2015; Kato et al. 2013, 2018). These comparisons are
89 for all-sky conditions (i.e. including any clouds). Irradiances under clear-sky conditions
90 are not explicitly separated from all-sky conditions in the evaluations. There are several
91 reasons that impede efforts at rigorous validation of clear-sky irradiances with surface
92 observations; 1) a clear-sky condition at a given site does not persist over a long time
93 (e.g. a month or longer), 2) there are mismatches of clear-sky conditions determined by

satellite- and ground-based instruments, and 3) field-of-view size between CERES instruments and ground-based radiometers differ.

Despite difficulties in evaluating computed clear-sky irradiances, they play an important role in quantifying aerosol and cloud radiative effects (Loeb and Su 2010; Soden and Chung 2017). Therefore, the uncertainty in surface irradiances need to be understood in order to assess the uncertainty in aerosol and cloud radiative effect. This work is the first attempt by the CERES team to evaluate clear-sky surface irradiances provided by its data products. One of the essential variables in computing clear-sky irradiances is aerosol optical depth. In this paper, we evaluate aerosol optical depth used for irradiance computations in the CERES project and analyze how the error propagates to clear-sky surface irradiances. Computations of surface irradiances provided by Edition 4.1 SYN1deg data products use aerosol optical depth derived by a chemical transport model [The Model for Atmospheric Transport and Chemistry (MATCH, Collins et al. 2001)] that assimilates MODIS-derived aerosol optical depth. In Section 2, we explain in the MATCH aerosol transport model and the assimilation of aerosol optical depth with MODIS. We then compare MATCH AOD to MODIS and MERRA2 aerosol products, as well as to AOD from the Aerosol Robotic Network (AERONET, Holben et al. 1998). Section 3 discusses differences found between the various estimates of AOD. Section 4 looks at clear sky surface irradiance calculations from the SYN1deg product compared to observed values and the impact of AOD and particle size on the results. Conclusions are presented in section 5.

2. Description of MATCH model

The Model for Atmospheric Transport and Chemistry (MATCH) is a transport model of intermediate complexity driven by offline meteorological fields from the National Centers for Environmental Prediction (NCEP) reanalysis. It is run on a 194×96 (1.9°×1.9°) spatial grid with a vertical resolution of 28 sigma-p levels. Temporally, the meteorological fields are linearly interpolated to 30-minute times at which time the chemical processes are run. One exception is that the sulfur model is interpolated again to run at 2-min subscale time steps. MATCH is one of the many aerosol transport models that participated in the AeroCom model inter-comparison project (Textor et al., 2006; Kinne et al. 2006; Textor et al. 2007) and the AeroCom carbon inter-comparison project (Koch et al., 2009; Huneeus et al., 2011).

Aerosol types included in MATCH are dust, sulfate, sea salt, soot, sulfates, carbon, and volcanic particles (**Table 1**). Model physics included in MATCH are parameterizations for convection and boundary layer processes that include prognostic cloud and precipitation schemes for aqueous chemistry and the scavenging of soluble species. MATCH also includes the ability to resolve the transport of aerosols via convection, boundary layer transport, and scavenging and deposition of soluble gases and aerosols. MATCH can simulate most cloud processes currently in use in a GCM (eg. cloud fraction, cloud water and ice content, fraction of water converted to rain and snow, and evaporation of condensate and precipitate). It also includes vertical turbulent eddy processes. These processes are then used for convective transport, wet scavenging, wet deposition and dry deposition of the MATCH aerosols. These various parameterizations were developed, originally, for the NCAR Community Climate Model (CCM) and

140 subsequently incorporated into the MATCH model. Descriptions of these
141 parameterizations are given by Rasch et. al (1997, 2001), Collins et. al (2001) and
142 additional papers described therein.
143 The MATCH aerosol suite includes a detailed mineral dust scheme in the Dust
144 Entrainment and Deposition model, (Zender et al., 2003), and a diagnostic
145 parameterization for sea-salt aerosol based on the 10m wind speed (Blanchard and
146 Woodcock, 1980). The sulfur cycle and the chemical reactions for sulfate aerosol creation
147 rely on monthly climatological oxidant fields and emission inventories (**Table 1**) for
148 sulfur oxides and oceanic dimethyl sulfide (photochemistry and nitrate aerosol are
149 omitted). The reaction scheme is similar to that of the Model for Ozone and Related
150 Chemical Tracers (MOZART), (Emmons et al., 2010). Carbon aerosols (both organic
151 compounds and soot) evolve with simple mean lifetime e-foldings from surface fluxes
152 specified through natural, biomass burning and fossil fuel burning emission inventories
153 (also monthly climatologies given in **Table 1**).
154

Table 1. Aerosol Types & Climatological Sources

Aerosol Type	*Source*	*Description*
Sea Salt	Blanchard and Woodcock, 1980	Wind Driven
Dust	Ginoux et al. (2001); Zender et al. (2003)	NCEP soil moisture, wind driven
Sulfate (natural & anthropogenic)	Benkovitz et al. (1996); Barth et al. (2000)	monthly climatological
Carbon (organic & Soot)	Liousse et al. (1996)	monthly climatological
Volcanic	Episodic inclusion of Sulfur dioxide	Processed by model

155
156 The optical properties of the various aerosol types (e.g. mass extinction
157 coefficient, single scatter albedo), which are key parameters for aerosol assimilation, are

158 drawn from the standard Optical Properties of Clouds and Aerosols (OPAC, Hess et al.
159 1998) database. However, scattering properties of maritime and dust aerosols used
160 in the radiative transfer calculations in the SYN1deg are not from MATCH. Instead,
161 aerosol types from MATCH are mapped to a similar set of scattering properties, per
162 Table 2, embedded in the Langley Fu & Liou radiative transfer (LFLRT) code (Fu and
163 Liou, 1993; Fu et. al 1998; Rose et. al 2013). These include OPAC as in MATCH for all
164 but the small and large dust particles. Dust scattering and absorption properties in the
165 LFLRT code are from Sinyuk et al. (2003).
166

Table 2. Mapping of MATCH aerosol types into Radiative Transfer code.

MATCH Constituent	Langley Fu & Liou Constituent	Langley Fu & Liou Spectral Properties
Sea Salt	Maritime	d'Almeida 1991
Hydrophobic Organic Carbon	Insoluble	OPAC
Hydrophilic Black Carbon Hydrophobic Black Carbon	Soot	OPAC
Hydrophilic Organic Carbon Tropospheric Sulfate	Water Soluble (WASO)	OPAC
Volcanic Stratospheric Sulfate	Suspended Organic (SUSO)	OPAC
Dust < 1.0μm	"Small" Dust	Sinyuk et al. (2003)
Dust 1.0 -2.5μm Dust 2.5-5.0 μm Dust 5.0-10.0 μm	"Large" Dust	Sinyuk et al. (2003)

167

168 **Figure 1** shows the single scatter albedo (SSA) and asymmetry parameter (ASY)
169 for the seven constituents in the LFLRT code at 500μm. Constituents with constant SSA
170 and/or ASY are given as numbers while those that vary with relative humidity are
171 plotted. The spectral properties for sea salt shown in Figure 1 were taken directly from

tables in d'Almeida et al., (1991). Note that the asymmetry parameter of maritime aerosol decreases with humidity. This is likely an error in the original Table A.30 of d'Almeida et al. (1991).

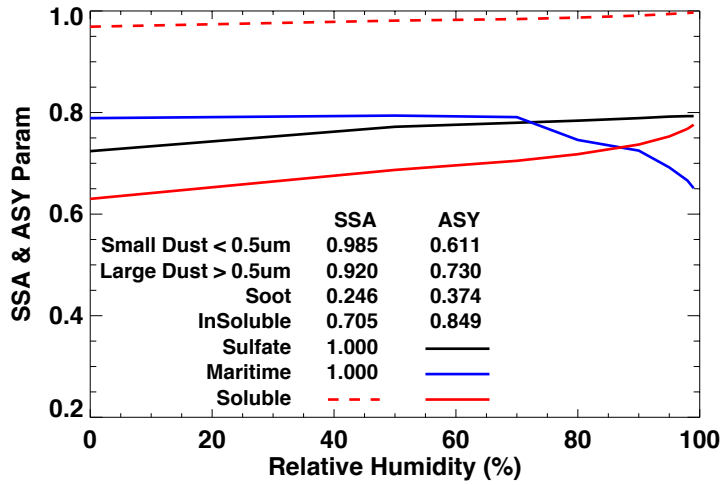

Figure 1. Single scatter albedo and asymmetry parameter for the seven aerosol types available in the Langley Fu & Liou Model SYN1deg calculations. Only those that vary with relative humidity are plotted. Others are listed as constants. All values are for properties at 550 μm.

2.1 MATCH Assimilation of MODIS Aerosol Optical Depths

One major advantage of the MATCH model is its ability to reliably assimilate satellite-based retrievals of aerosol optical depth (AOD) to constrain the climatologically forced aerosols generated within the chemical transport portion of the code. Edition 4 MATCH algorithms ingest MODIS Collection 6.1 AOD (Remer et al., 2005), beginning in March 2000 from the Terra satellite and June 2002 from both Terra and Aqua satellites. The MATCH assimilates MODIS AOD at the green wavelength of 550 nm. MATCH combines AOD derived by the Dark Target (Levy et al. 2013) and Deep Blue algorithms (Hsu et al., 2006). A global daily mean AOD in a 1.9°x1.9° grid is derived from Terra and Aqua observations by simply averaging available Terra and Aqua dark

target and deep blue derived AODs in a grid box. Unlike dark target and deep blue merged product (MOD08), we do not use a quality assurance confidence (QAC) score to screen AOD.

The assimilation process begins by combining the dark target and deep blue AOD from MODIS (both Terra and Aqua when available) and creating daily averages. As MATCH progresses through time the AOD at local solar noon are assimilated by taking a 15° longitude width of retrieved AOD from the daily mean map. Examples of the magnitude of AOD adjustments by the assimilation are shown in **Fig. 2. Figure 2a** shows hourly AOD field differences, 4 UT minus 3 UT on February 1st, 2020. Similarly, **Figure 2b** shows 10 UT minus 9 UT of the same day. The 15° vertical band is clearly visible where red (blue) colors indicate total column aerosol is increased (decreased) by the MODIS AOD assimilation. Following the AOD adjustment, aerosol masses in the atmospheric column through the troposphere are scaled to closely match the AOD derived from MODIS. Neither the vertical profile nor the relative abundance of the aerosol species is adjusted. Once aerosol mass is adjusted at the local noon for the regions where MODIS AOD is available, the adjusted aerosol mass is carried on to the next time step. Besides the MODIS adjustments, wind driven sea-salt creation and deposition are found along frontal boundaries in the North Atlantic and Southern Oceans. The maps also indicate hourly increases and decreases in high aerosol loading areas such as those found around China and SE Asia. Episodic events such as intense fires or volcanic eruptions are not specifically included in the MATCH aerosol package. Such events are captured by the assimilation of MODIS AOD and total column aerosol loading is adjusted upward. The adjustment is applied to AOD only. The aerosol type (and so scattering properties) is

not adjusted to reflect the reality of the scattering or absorbing aerosol during such an event.

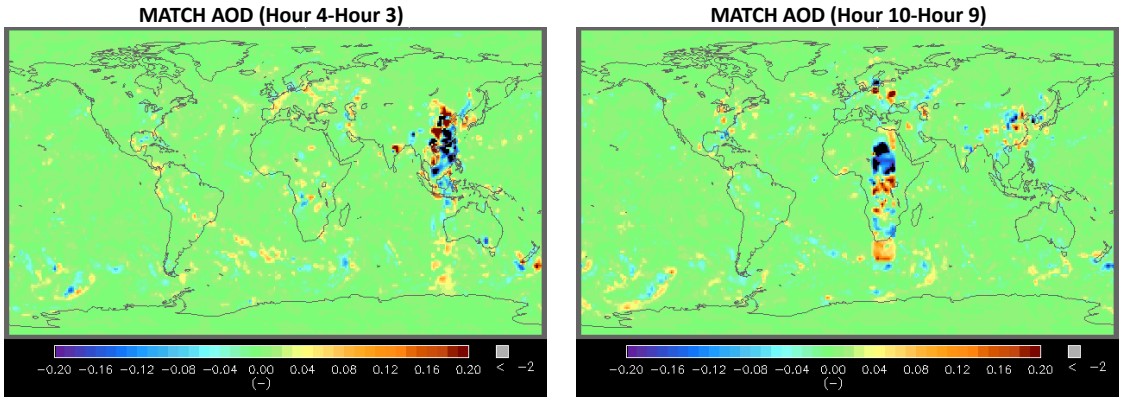

Figure 2. Difference of MATCH AOD due to the assimilation of MODIS AOD. The left plot is 4 UT minus 3 UT and right plot is 10 UT minus 9 UT on February 1, 2020. AOD is adjusted at the local solar noon within the 15° longitudinal band by the MODIS AOD assimilation. Wind-blown dust and sea salts differences are also apparent outside the 15° longitudinal band.

2.2 MATCH and MERRA2 comparison

In this section, we compare AODs between MATCH and MERRA2 (Randles et al., 2017) in which MODIS clear-sky radiances are assimilated. MERRA2 also assimilates surface observed AOD by AERONET and ship born AOD observations as well as AVHRR and MISR retrievals for the years 2000-2002 and 2000-2014 respectively. We compare AODs in two different ways. First, MATCH and MERRA2 AODs are compared with MODIS AODs. The first comparison tests the consistency of daily means when MODIS aerosol optical depth is available (i.e. clear somewhere in the grid box at Terra and Aqua overpass time). Second, MATCH and MERRA2 AODs are compared under all-sky conditions, which is only possible with modeled AODs.

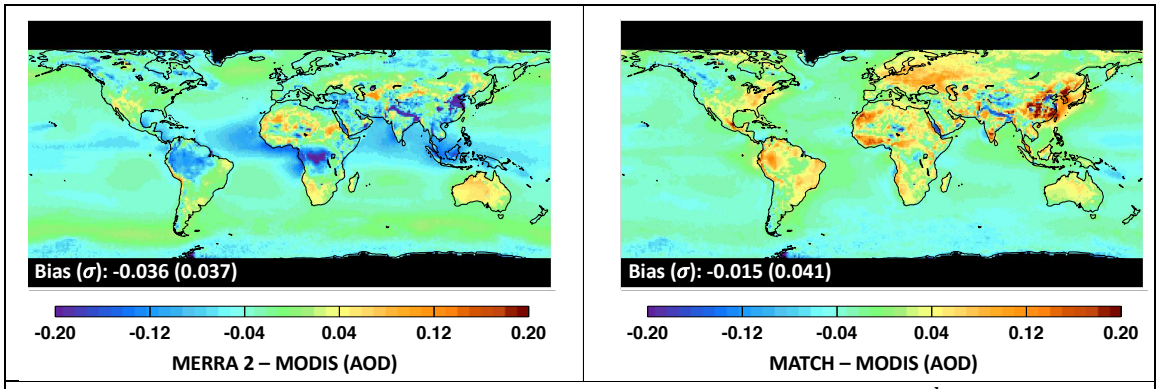

Figure 3: Climatological mean aerosol optical depth (AOD, i.e. $\langle AOD_{MODIS}^{clr} \rangle$ see texts for the definition) difference of left) MERRA2 – MODIS and right) MATCH – MODIS averaged over Mar 2000 through Feb 2020. MERRA2 and MATCH daily mean AODs are sampled when daily mean MODIS AOD from the same 1°×1° grid is available. Sampled daily mean AODs are subsequently averaged. MODIS AODs are averages of MODIS dark target and deep blue algorithms from both Terra (MOD08) and Aqua (MYD08) data products.

Figure 3 shows differences of climatological mean AOD between MERRA2 and MODIS on the left and MATCH and MODIS on the right. To compute the monthly mean AOD differences, both MERRA2 and MATCH daily mean AODs are sampled when daily mean MODIS AOD (MODIS products MOD08 and MYD08) from the same 1°×1° grid is available (hereinafter AOD_{MODIS}^{clr}). Sampled daily mean AODs (AOD_{MODIS}^{clr}) are subsequently averaged (hereinafter $\langle AOD_{MODIS}^{clr} \rangle$, where the bracket indicates a simple arithmetic mean). Although both products assimilate MODIS observations, each shows fairly significant differences from MODIS values. Differences arise because MODIS daily mean AOD is clear sky at Terra and Aqua overpass time while MERRA2 and MATCH daily mean AOD includes AOD from other times of the day. When the non-overpass time is also clear, MATCH AOD_{MODIS}^{clr} should be close to MODIS AOD_{MODIS}^{clr}. However, when clouds are present in MATCH during non-overpass times, modeled AOD are used, hence the daily mean AOD can deviate from MODIS AOD_{MODIS}^{clr}. In addition,

AOD differences for MERRA2 at Terra and Aqua overpass times might be larger than MATCH even for clear-sky conditions as MERRA2 assimilates observed AOD data other than MODIS AOD when and where these events might occur.

While MATCH shows large positive differences over land, especially China and southeast Asia, Australia, Amazon, and north Africa, MERRA2 shows significant negative differences over major rain-forest regions of south America, Africa, and the tropical western Pacific. Both products are closer to MODIS AOD over ocean compared to $\langle AOD_{MODIS}^{clr} \rangle$ over land except MERRA2 shows a negative difference across the Indian ocean and off the west coast of Africa in the Atlantic Ocean. When MODIS AOD_{MODIS}^{clr} is available in the grid box, MATCH weighs MODIS AOD heavily in its assimilation at local solar noon so that MATCH AOD is nearly identical to MODIS AOD at the local noon under clear-sky regions. Consequently, the difference of climatological global mean MATCH and MODIS AOD_{MODIS}^{clr} (-0.015) is smaller than the difference of MERRA2 and MODIS AOD_{MODIS}^{clr} (-0.036).

Figure 4 shows the difference of AOD_{MODIS}^{clr} more clearly. In **Fig. 4** AOD_{MODIS}^{clr} are compared directly in a log-density plot where each point represents a comparison for the daily average of a given grid box; MERRA2 versus MODIS on the left and MATCH versus MODIS on the right. **Figure 4** indicates that MATCH AOD_{MODIS}^{clr} has a smaller bias with respect to the MODIS AOD than the MERRA2 AOD but has approximately the same RMS compared to the MERRA2 AOD_{MODIS}^{clr}.

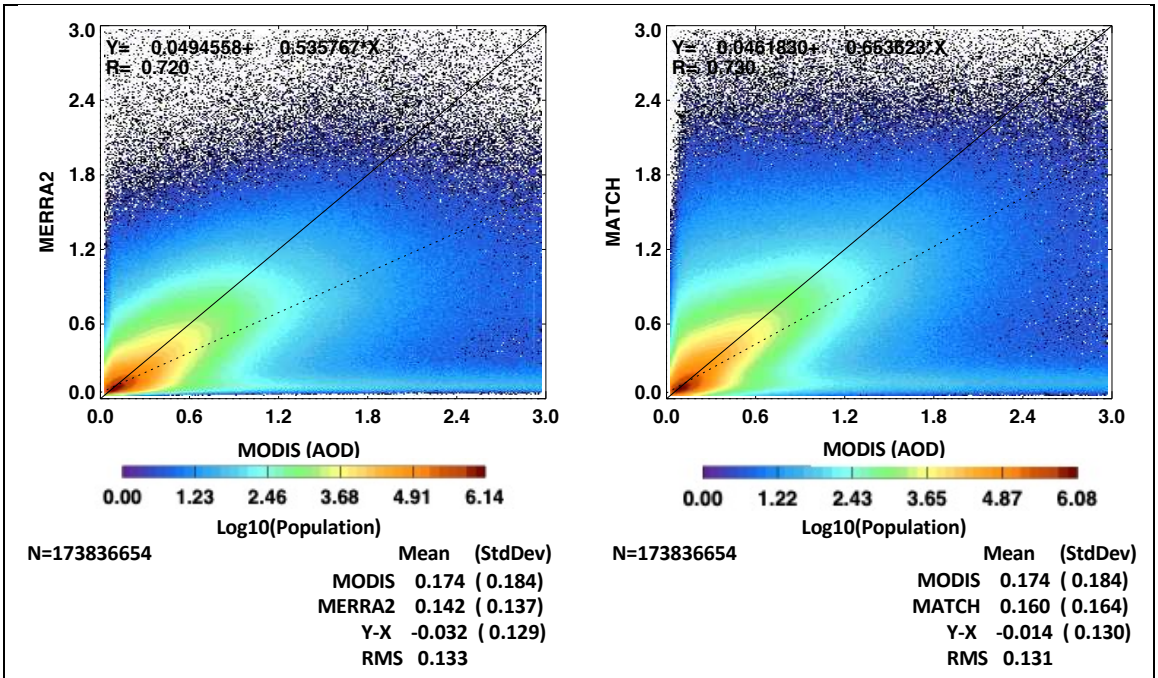

Figure 4: Scatter plot of daily 1°×1° mean aerosol optical depth from a) MERRA2 and b) MATCH versus AOD derived from MODIS on Terra and Aqua for Mar 2000 through Feb 2020. MODIS AODs are 1°×1° daily averages derived by the dark target and deep blue algorithms. Only days and grid boxes that have MODIS AOD (i.e. AOD_{MODIS}^{clr} defined in the texts) are used.

We now consider more directly, differences between the MATCH and MERRA2 climatological AOD fields for all-sky and *estimated* clear sky conditions. **Figure 5** shows 1°×1° climatological mean maps of MATCH AOD on the left and its difference from MERRA2 on the right for all sky (top maps) and estimated clear sky (bottom maps) conditions for March 2000 through February 2020. A clear-sky area weighted monthly mean aerosol optical depth is derived by averaging daily mean aerosol optical depth weighted by clear fraction (hereinafter $\overline{AOD_{MODIS}^{clr}}$, overbar indicates monthly mean), where the clear fraction is derived from MODIS on Terra and Aqua (Loeb et al. 2020, Minnis et al. 2020). MATCH all-sky AOD (hereinafter $\overline{AOD^{all}}$) is larger than MERRA2 $\overline{AOD^{all}}$), particularly over the rain forest regions of the globe as well as India and China.

Although the difference is smaller, the difference of $\overline{AOD_{MODIS}^{clr}}$ shows a similar spatial pattern (**Fig. 5** bottom right) to the all-sky difference. This is consistent with **Fig. 3**, showing that MERRA2 AOD_{MODIS}^{clr} underestimates AOD with respect to MODIS AOD_{MODIS}^{clr}. A larger difference in MATCH AOD over convective regions (e.g. Amazon, central Africa, and south east Asia) is caused by how dark target and deep blue AOD are merged. As mentioned earlier, we do not use QAC to screen AOD. Convective clouds introduce a larger uncertainty to AOD because of a 3D radiation effect or poor fit to observations with retrieved AOD (personal communication with R. Levy 2020). For these situations, AODs associated with QA confidence scores less than 2 are screened out in the MOD08 dark target and deep blue merged product (Levy et al. 2013).

2.3 Comparison with AERONET

The above results indicate that both MATCH AOD_{MODIS}^{clr} and MERRA2 $\overline{AOD_{MODIS}^{clr}}$ are generally smaller than MODIS $\overline{AOD_{MODIS}^{clr}}$. Larger difference between MATCH and MERRA2 $\overline{AOD^{all}}$ over convective regions originated from merged AOD product used for the assimilation. Of primary importance to radiative transfer calculations within the SYN1deg product is the ability of the MATCH model to accurately represent total column aerosol optical depth. To test the overall accuracy, we use observations from the AERosol RObotic NETwork (AERONET). AERONET is a global federation of ground-based remotes sensing sites developed by NASA and now supported by a number of institutions around the world (Holben et al. 1998). Each site maintains a CIMEL sun-photometer that scans the daytime sky every 20 minutes. Collected data are processed according to standards of calibration and processing maintained by the AERONET

project. Here we utilize Level 2.0, data that have been screened for clouds and quality assured (Smirnov et al. 2000).

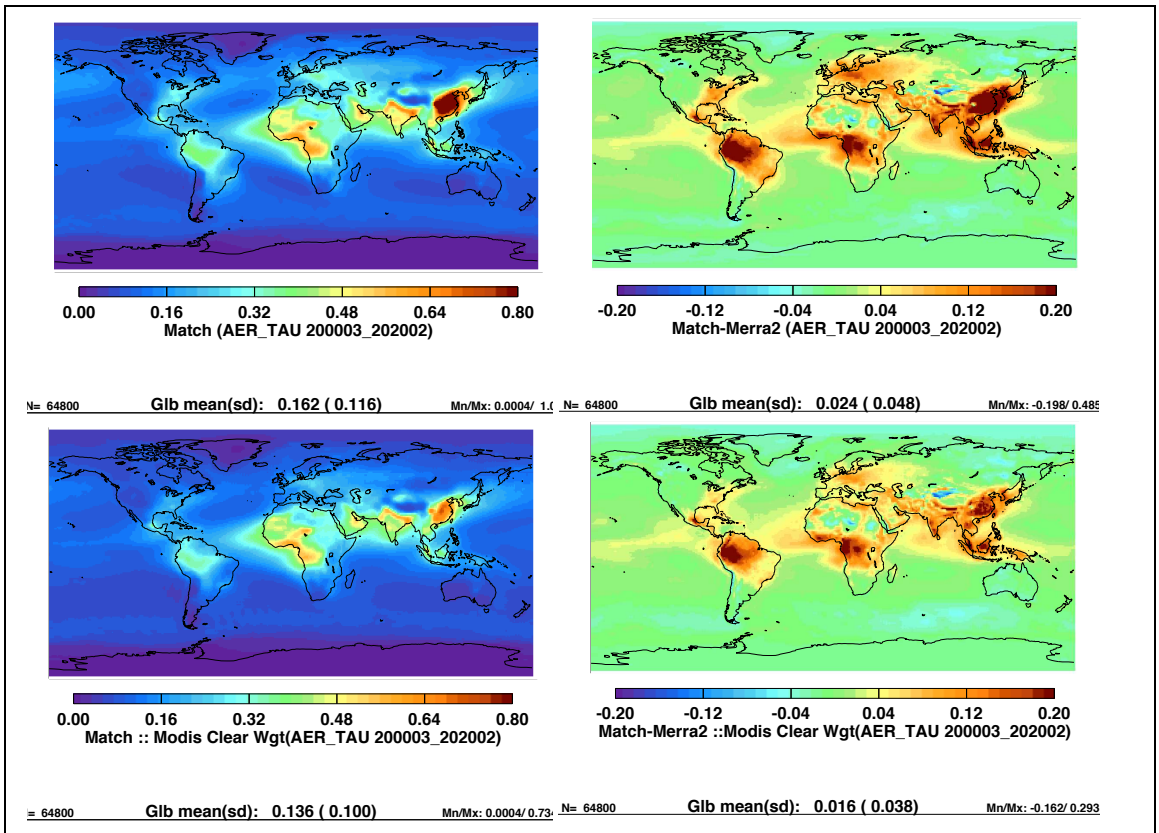

Figure 5. Left) Climatological mean AOD from MATCH and right) the difference between MATCH and MERRA2 (MATCH – MERRA2). Top maps are for all-sky (AOD^{all}_{MODIS}), bottom maps are clear-sky area weighted average of AOD (AOD^{clr}_{MODIS}). Clear-sky weighted monthly mean AOD is derived by averaging daily mean aerosol optical depth weighted by daily 1°×1° gridded mean clear fraction where the clear fraction is derived from MODIS based cloud fraction on Terra and Aqua.

Figure 6 shows an hourly time series of AOD from MATCH, MERRA2 and AERONET for January 2010 at the Beijing China AERONET site. The top plot shows cloud fraction time series derived from MODIS and GEOs from the SYN1deg Ed4.1 product (Rutan et al. 2015), and the bottom plot shows AOD time series. Generally, both models produce a large variability of AOD at this site fairly well over the course of the

month. While both MERRA2 and MATCH AODs increase near times when cloud fraction approaches 100%, the increase of MATCH AOD, which correlates with the increase of AERONET AOD relatively well, is larger than the increase of MERRA2 AOD. Although the temporal correlation coefficient of the MATCH and AERONET AODs is smaller at this site during summer months than during winter months (not shown), a good temporal correlation between MATCH and AERONET AODs is consistent across most locations and times we considered. To show this statistically, in the following, we extend this analysis to a number of AERONET sites grouped geographically based on general aerosol type.

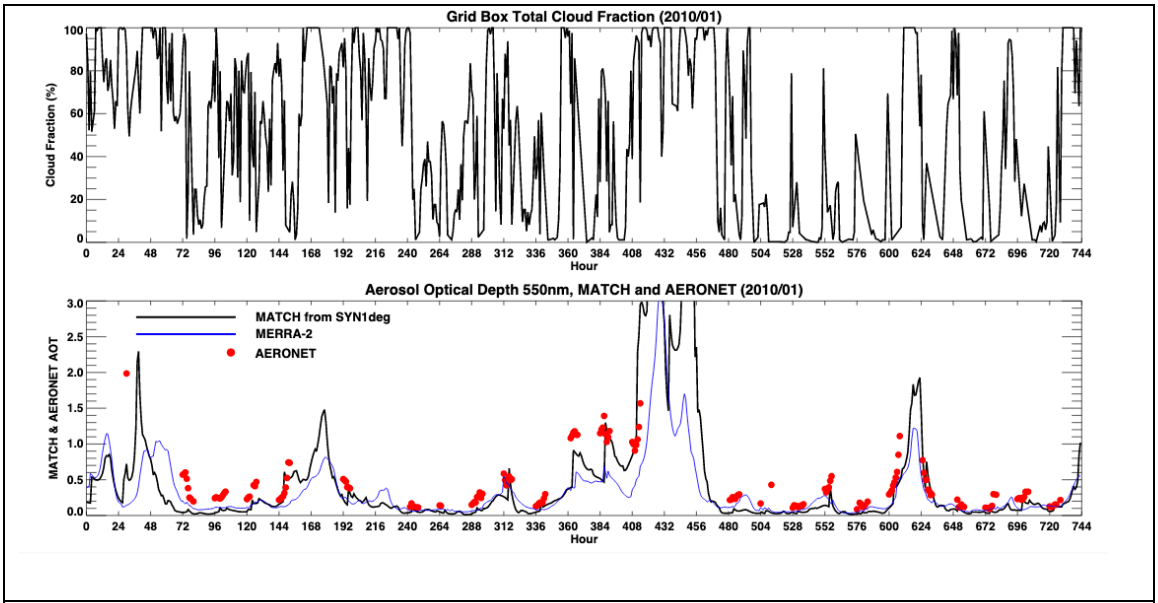

Figure 6. Hourly time series of grid box cloud fraction (top) from SYN1deg Ed4.1 CERES product and AOD (bottom). Results are from the grid box containing the AERONET Beijing, CH site. Black line MATCH, blue line MERRA-2, red dots, AERONET observations. MATCH and, to a lesser degree MERRA-2 often have large increases in AOD when cloud fraction nears 100%.

Aerosol optical depths from AERONET are nominally provided at 8 spectral channels, every 20 minutes given favorable conditions. We use two channels to derive

observed AOD at 550 nm to compare to the AOD provided by the MATCH model. Because the SYN1deg radiative transfer calculation is done hourly, we average any observations within a given hour period centered at the 30th minute for each site collocated within a SYN1deg grid box. AERONET sites chosen are shown in **Figure 7** with a complete listing of all sites in Appendix 1. Though we examine 55 sites over 20+ years, we aggregate the statistics within continental regions which naturally isolates them by general climatic conditions. Tables 3 and 4 show comparisons for each site grouping, respectively, for clear sky (less than 1% cloud identified by MODIS and geostationary satellites in the SYN1deg grid box) conditions and for all sky (any cloud condition within the SYN1deg grid box) conditions. Using clear-sky scenes identified by MODIS only gives the same statistical results with fewer number of samples. Statistics shown in Tables 3 and 4 are the average observed value, mean bias (MATCH – Observation), root mean square (RMS) difference and the correlation coefficient (R) over the time period from March 2000 through February 2020. The actual time period varies depending on the site due to AERONET data availability. The RMS difference and correlation coefficient are computed by each site with hourly mean values where observations are available from March 2000 through February 2020. For comparison purposes we show the same statistics derived from observations compared to MERRA2 AODs using the identical hours. We note, however, that MERRA2 assimilates AERONET while MATCH AODs are independent from AERONET AODs. MATCH AOD for the Brazil group is biased high by 0.02, and the China/Korea group has no appreciable bias compared with AERONET AODs. These two regions have relatively large bias of $\langle AOD_{MODIS}^{clr} \rangle$ from

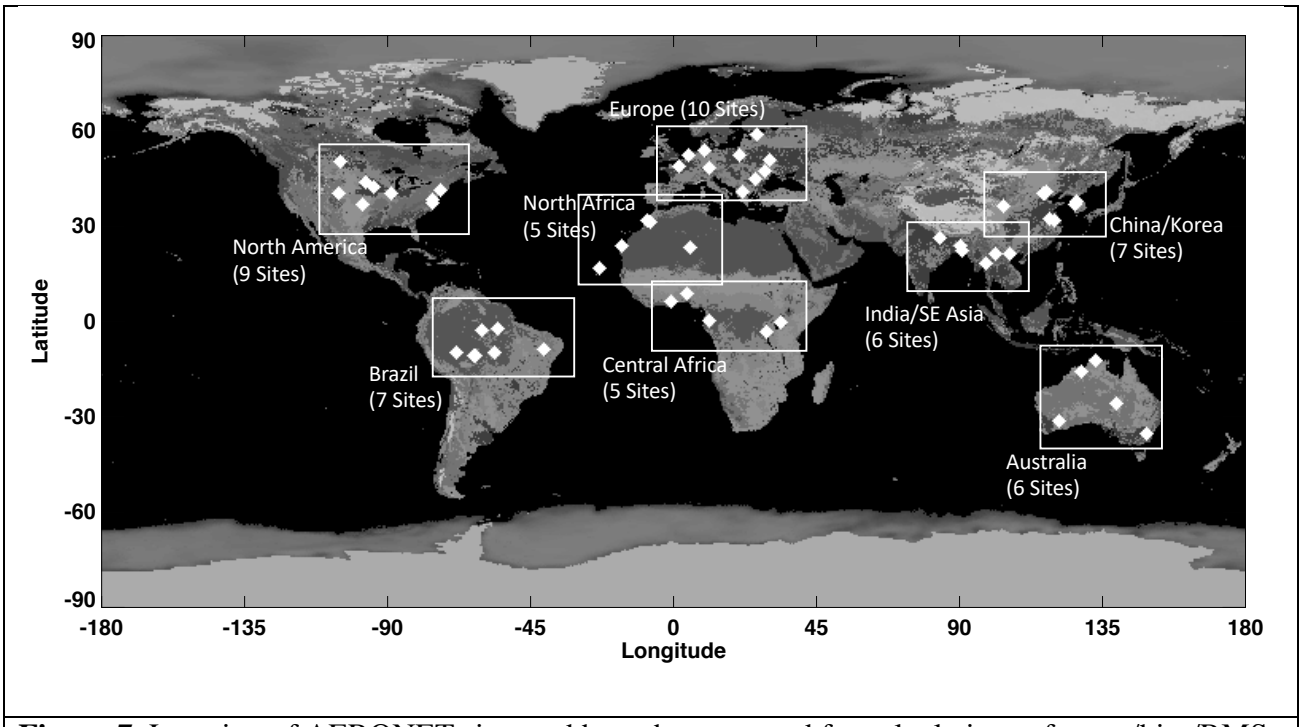

Figure 7. Location of AERONET sites and how they grouped for calculations of mean/bias/RMS with respect to MATCH and MERRA-2 optical depths found in tables 3 and 4.

MATCH compared with MODIS AODs (**Fig. 3** right). In contrast, negative bias of MERRA2 AODs compared with AERONET AODs for Brazil, central Africa, and China/Korea groups are consistent with negative bias of MERRA2 $\langle AOD_{MODIS}^{clr} \rangle$ compared with MODIS AODs (**Fig. 3** left). For the China/Korea group, the RMS difference between MATCH AODs and AERONET AODs is 0.18 and correlation coefficient is 0.7. These are worse than the counterpart values of MERRA2 versus AERONET AODs because summertime agreement between MATCH and AERONET AODs is worse if a similar plot as **Fig. 6** is plotted for summertime when hygroscopic aerosols are dominant under high relative humidity conditions.

The sign of the MATCH AODs compared to AERONET AODs for all-sky conditions is generally consistent with the sign of clear-sky counterparts. The RMS difference under all-sky conditions is generally larger than the clear-sky RMS difference

while the correlation coefficient is nearly the same. The biases for MERRA2 comparisons are generally comparable to MATCH though RMS for MERRA2 tend to be slightly smaller and correlations tend to be higher due in part to the assimilation of AERONET into the MERRA2 model.

Table 3. Hourly AERONET station statistics for MATCH and MERRA-2. Continental Groups, Clear Sky conditions[1]

				MATCH			MERRA-2		
Site	Predominant Aerosol Type	Number	Observed Average	Bias	RMS	R^2	Bias	RMS	R^2
Australia (5 Sites)	Dust Smoke	20925	0.06	0.01	0.06	0.4	0.03	0.05	0.7
Brazil (7 Sites)	Smoke Polluted	6554	0.14	0.02	0.10	0.8	-0.02	0.08	0.9
Central Africa (5 Sites)	Smoke	2139	0.70	-0.10	0.24	0.9	-0.10	0.24	0.9
North Africa (5 Sites)	Dust	10047	0.17	0.07	0.15	0.7	0.02	0.10	0.8
China/Korea (8 Sites)	Polluted	2827	0.26	-0.00	0.18	0.7	-0.03	0.15	0.8
India/SE Asia (6 Sites)	Smoke Polluted	3010	0.51	-0.09	0.28	0.6	-0.10	0.24	0.8
North America (9 SIte)	Continental Polluted	21429	0.10	-0.00	0.07	0.7	0.00	0.06	0.8
Europe (10 Sites)	Continental Polluted	10211	0.13	0.01	0.07	0.7	-0.02	0.05	0.8

[1]The time period used is from Mar 2000 through Apr 2020. Actual period varies by site depending on AERONET data availability. Clear Sky is identified by MODIS and geostationary satellites and the cloud fraction is less than 1% over a SYN1deg grid box.

Results for all points across all sites and times are shown in **Figure 8**. The color density plots are in log scale and indicate the vast majority of observations have an AOD of less than one for both clear and all sky conditions observed within the SYN1deg grid box. Biases are less than 10% of the mean value but RMS is large relative to the mean observed value. Overall correlation is approximately 0.8. The 'clear sky' hours (where SYN1deg estimated less than 1% cloud in the grid box based on MODIS and GEO

observations) is a little more than 10% of the overall points. When MATCH AOD is compared to MERRA2 AOD (not shown) MATCH is biased approximately 10% higher.

Table 4. Hourly AERONET station statistics for MATCH and MERRA-2.
Continental Groups, All Sky Conditions[1]

				MATCH			MERRA-2		
Site	Predominant Aerosol Type	Number	Observed Average	Bias	RMS	R^2	Bias	RMS	R^2
Australia (5 Sites)	Dust Smoke	110523	0.09	0.00	0.09	0.5	0.02	0.07	0.8
Brazil (7 Sites)	Smoke Polluted	72656	0.25	0.03	0.23	0.8	-0.04	0.18	0.9
Central Africa (5 Sites)	Smoke	41193	0.55	-0.07	0.26	0.8	-0.10	0.26	0.9
North Africa (5 Sites)	Dust	43205	0.23	0.08	0.20	0.7	0.01	0.14	0.8
China/Korea (8 Sites)	Polluted	52287	0.45	0.01	0.31	0.7	-0.08	0.27	0.8
India/SE Asia (6 Sites)	Smoke Polluted	44534	0.61	-0.06	0.32	0.6	-0.10	0.32	0.7
North America (9 Sites)	Continental Polluted	160356	0.13	0.02	0.13	0.6	0.00	0.09	0.7
Europe (10 Sites)	Continental Polluted	175010	0.18	0.04	0.14	0.6	-0.02	0.08	0.8

[1] The time period used for the statistics is from March 2000 through April 2020. Total sample varies by site depending on AERONET data availability.

3. Discussion of AOD Differences

In this section, we investigate the reason for the AOD differences shown in the previous section. In addition, we estimate the effect of the AOD differences to surface irradiances when MATCH AODs are used for surface irradiance computations. Generally, cloud contamination in MODIS AODs is caused by unresolved sub-pixel scale clouds (Kaufman et al. 2005; Martins et al. 2002). The difference shown over convective regions, therefore, seems to be caused by the uncertainty due to 3D radiative effects that impact retrieved AODs by unknown amounts (Wen et al. 2007), by errors in estimating

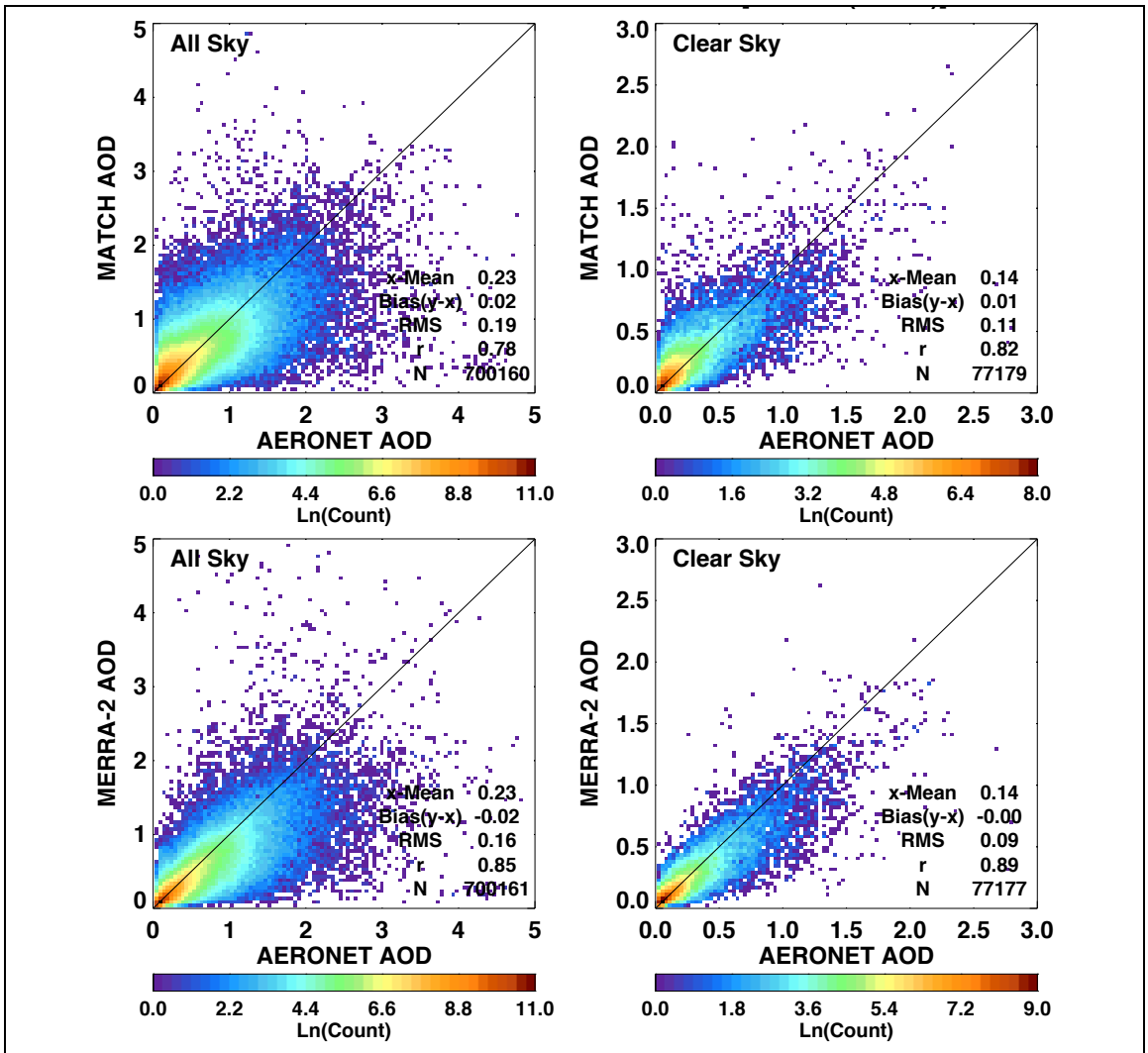

Figure 8. All sky (left) and clear sky (right) comparisons of observed (AERONET) hour mean optical depths to estimates from the MATCH model for 20+ years at 55 AERONET sites shown in **Fig 7**.

373

374 the fraction of hygroscopic aerosols or by the errors in estimating water uptake by

375 hygroscopic aerosols (Su et al 2008, Marshak et al., 2021). Larger AODs are screened out

376 in the MOD08 data product while the CERES team uses all retrieved AODs regardless of

377 the QAC score, likely increasing MATCH AOD overall. The comparison with

378 AERONET AODs is not decisive to determine how to screen MODIS AODs because

379 MATCH AODs are positively biased and MERRA2 AODs are negatively biased for the

Brazil group. The result underscores the difficulty of deriving accurate AODs, which appear to involve requirements in addition to identification of clear-sky scenes. Levy et al. (2013) list reasons lowering the QAC score as 1) pixels are thrown out due to cloud masking, 2) retrieval solution does not fit the observation well, and 3) the solution is not physically plausible given the observed situation. Therefore, even though the difficulty of identifying clear-sky scenes is driven by cloud contamination by trade cumulus (Loeb et al. 2018), the difficulty of deriving AODs exists over convective regions (Varnai et al., 2017) as well.

Larger positive biases of MATCH AODs compared with AERONET AODs exist over Africa (Tables 3 and 4). For North Africa, the bias is known to be caused by excessive dust generated by the MATCH algorithm. Even though modeled aerosols are not often used over north Africa owing to the abundance of clear-sky conditions, the dust problem leads to a larger positive AOD bias. In addition, MATCH uses fixed aerosol sources in time. Therefore, it tends to miss large aerosol events, such as forest fires, until clear-sky conditions occur, allowing observations of the event by MODIS. This leads to a larger RMS difference and lower correlation coefficient with AERONET AODs compared with those from MERRA2 versus AERONET.

Because MODIS AOD are not generally available under overcast conditions, the reliance on modeled AOD increases as the cloud fraction over a 1°×1° grid increases. **Figure 6**, which shows that AERONET AOD increases with cloud fraction derived from satellites, indicates that as the cloud fraction over a 1°×1° grid increases, AOD over the clear-sky portion of the grid increases. In addition, **Fig. 6** suggests that modeled AODs under near overcast conditions are significantly larger than clear-sky AODs that are

403 constrained by MODIS observations. Because we are unable to evaluate AODs for
404 overcast conditions, here we assess AOD changes with cloud fraction using ground-based
405 observations. **Figure 9** shows the distribution of AERONET AODs for clear-sky and all-
406 sky conditions, as well as precipitable water derived from a microwave radiometer
407 separated by these two conditions. Clear-sky is identified by the Long-Ackerman
408 algorithm (Long et al. 2006) that uses surface direct and diffuse irradiances. **Figure 9**
409 shows that AOD and precipitable water under all-sky conditions are significantly larger

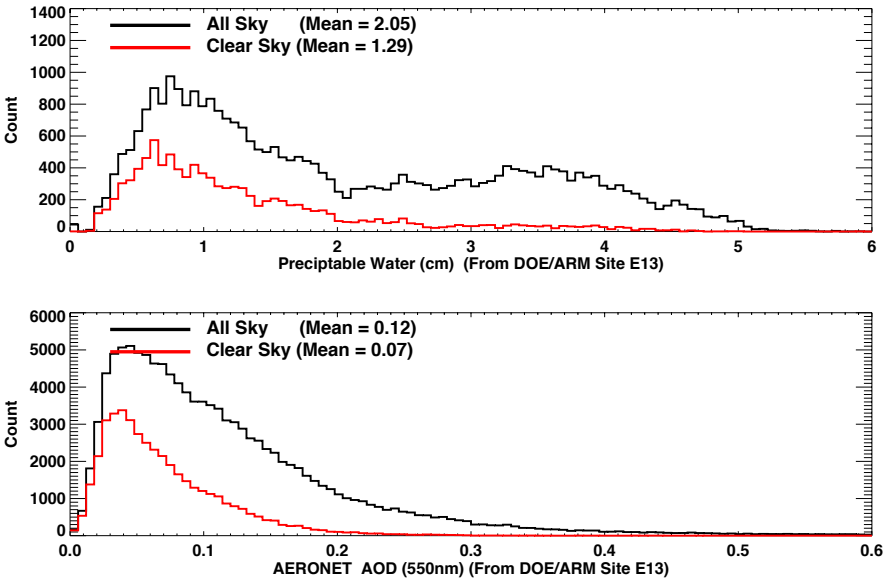

Figure 9. a) 15-minute mean precipitable water distributions from Microwave radiometer observations at ARM/SGP E13 site under all sky and clear sky conditions. b) 15-minute mean aerosol optical depth distributions from AERONET sun-photometer at 550nm. 'Clear sky' is here defined as when a 15-minute time period where the SWFA, surface radiometry-based cloud fraction, equals 0.

410

411 than those under clear-sky conditions. When we use cloud fraction derived from satellite
412 and plot AOD and precipitable water as a function of the cloud fraction using the same
413 grid box where the ground site is located, AOD and precipitable water increase with the
414 cloud fraction (**Fig. 10**). Therefore, increasing AOD with cloud fraction shown in **Fig. 6**

415 is qualitatively explained by increasing AOD of hygroscopic aerosols with relative
416 humidity. However, **Fig. 10** indicates that either the growth of MATCH AOD is too
417 strong or modeled MATCH AOD under all-sky conditions is too large.

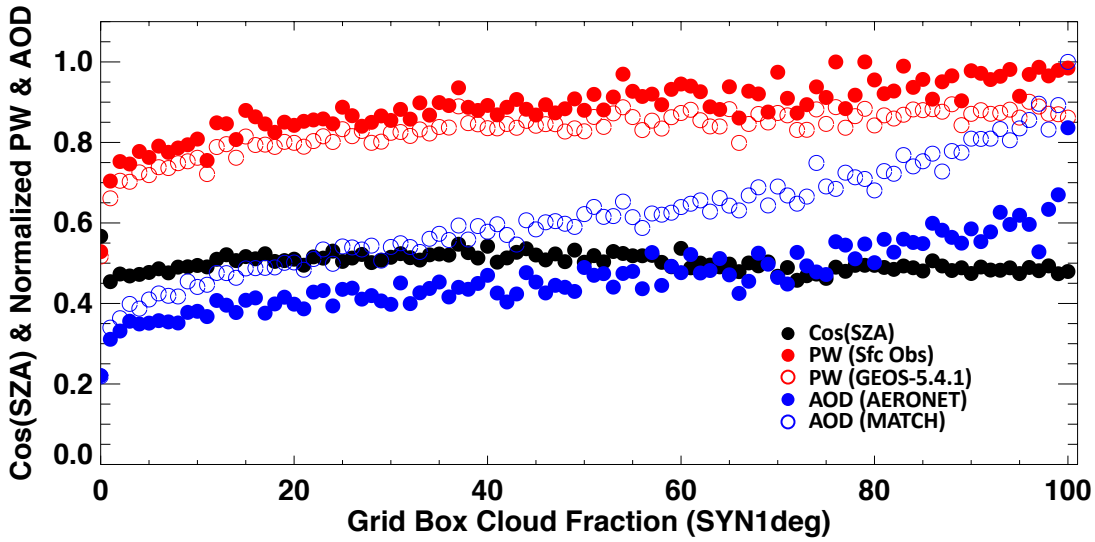

Figure 10. Aerosol optical depth (AOD) and precipitable water (PW) as a function of cloud fraction over the 1°×1° grid box where the ARM/SGP E13 and SURFRAD Bondville IL sites are located. Closed and open blue circles are, respectively, AOD derived from AERONET and MATCH AOD. Closed and open red circles are, respectively, PW derived from microwave radiometer and CIMEL sun photometer and GEOS-5.4.1 PW. Cloud fractions are derived from MODIS and geostationary satellites. Black dots are mean cosine solar zenith angle of the time of AOD and PW observations. AOD and PW are normalized to their maximum value for display.

418

419 ## 4. Clear Sky Comparisons of SYN1deg and Surface Observed Irradiances

420 We consider the impact of MATCH aerosols on computed surface irradiances by
421 comparing calculated hourly mean surface downward irradiances from the Ed4.1
422 SYN1deg-Hour product to observations of downward irradiance. In a 1°×1° grid box
423 with an approximate size of 111 km^2, 100% clear sky sampled over one hour as
424 determined by MODIS or geostationary satellites is relatively rare. None the less, by
425 grouping sites based on general surface conditions and analyzing 20 years of data

sufficient samples are found. **Figure 11** shows the sites, grouped by color, including 15 land sites labeled "Mid-Latitude" (Green), 6 sites labeled "Desert" (Red), 6 sites labeled "Polar" (White) and 46 buoys (Blue). Surface observed SW irradiance from the land sites comes from the Baseline Surface Radiation Network (Ohmura et al. 1998; Dreimel et al. 2018) and buoy data are made available

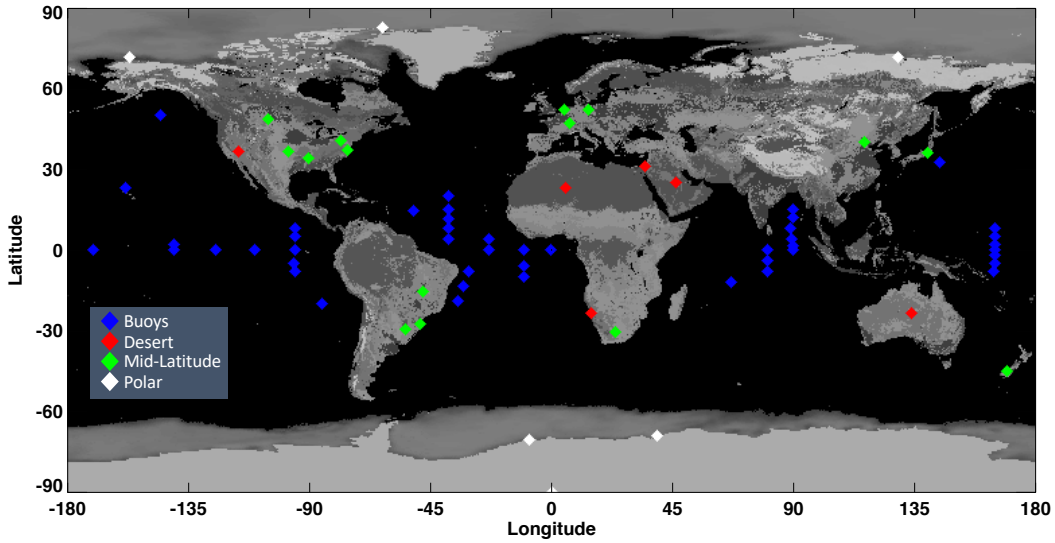

Figure 11. Location of surface observations of downwelling shortwave irradiance used to compare the SYN1deg Ed4.1 calculations to observations for all available hours (from Mar 2000 through Dec 2019) where the SYN1deg cloud analysis determines the hour and grid box to be 100% clear sky.

from the Pacific Marine Environmental Lab (PMEL) (McPhaden et al. 2002, 2009) and the Woods Hole Oceanographic Institute (WHOI) (Colbo and Weller, 2009). A complete listing is given in Appendix A.

4.1 Shortwave Comparisons

We begin with a simple sensitivity calculation of AOD on surface Downward Shortwave Irradiance (DSI). **Figure 12** shows a series of radiative transfer calculations using the "On-Line Langley Fu & Liou radiative transfer code

(https:// cloudsgate2.larc.nasa.gov/cgi-bin/fuliou/runfl.cgi) with an open shrub spectral albedo (broadband albedo of 0.14 at μ_0=1.0), "continental" aerosol, and no clouds. Values on the solid black line are calculated DSI with an AOD of 0.09 at six different solar zenith angles. Calculations were then done for AODs of 0.0 and 0.18, at the same solar zenith angles, representing 100% error bounds of mean AODs derived from AERONET as found in Tables 3 and 4 for the Australia sites where the RMS is approximately equal to the observed average of AOD. Orange and red shaded areas indicate potential bias of DSI at a given solar zenith angle. Irradiance values scale nearly linearly with Cos(SZA) between these limits. **Figure 12** shows the error remains nearly constant until a μ_0=0.5 where it begins to decrease as insolation decreases. However, due to small downward irradiances at large solar zenith angles, the percentage error increases.

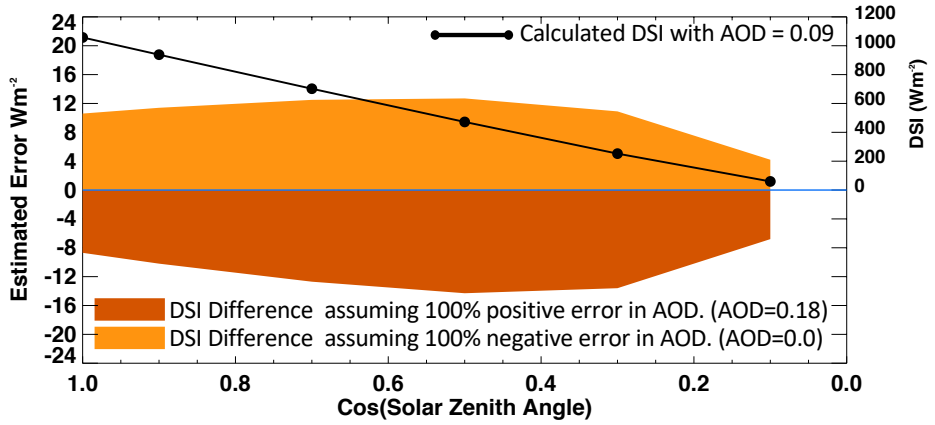

Figure 12. Calculated DSI error at the surface computed with the LFLRT model due to the error in AODs. AOD is assumed to be 0.09. Light and dark orange envelope indicate, respectively, positive and negative errors in Wm-2 (left axis) due to 100% AOD errors. Envelopes are computed with AODs of 0.0 (a -100% error) and 0.18 (a +100% error), at the same solar zenith angles, representing 100% error bounds. Values on the solid black line are calculated DSI (right axis) with an AOD = 0.09 at six solar zenith angles.

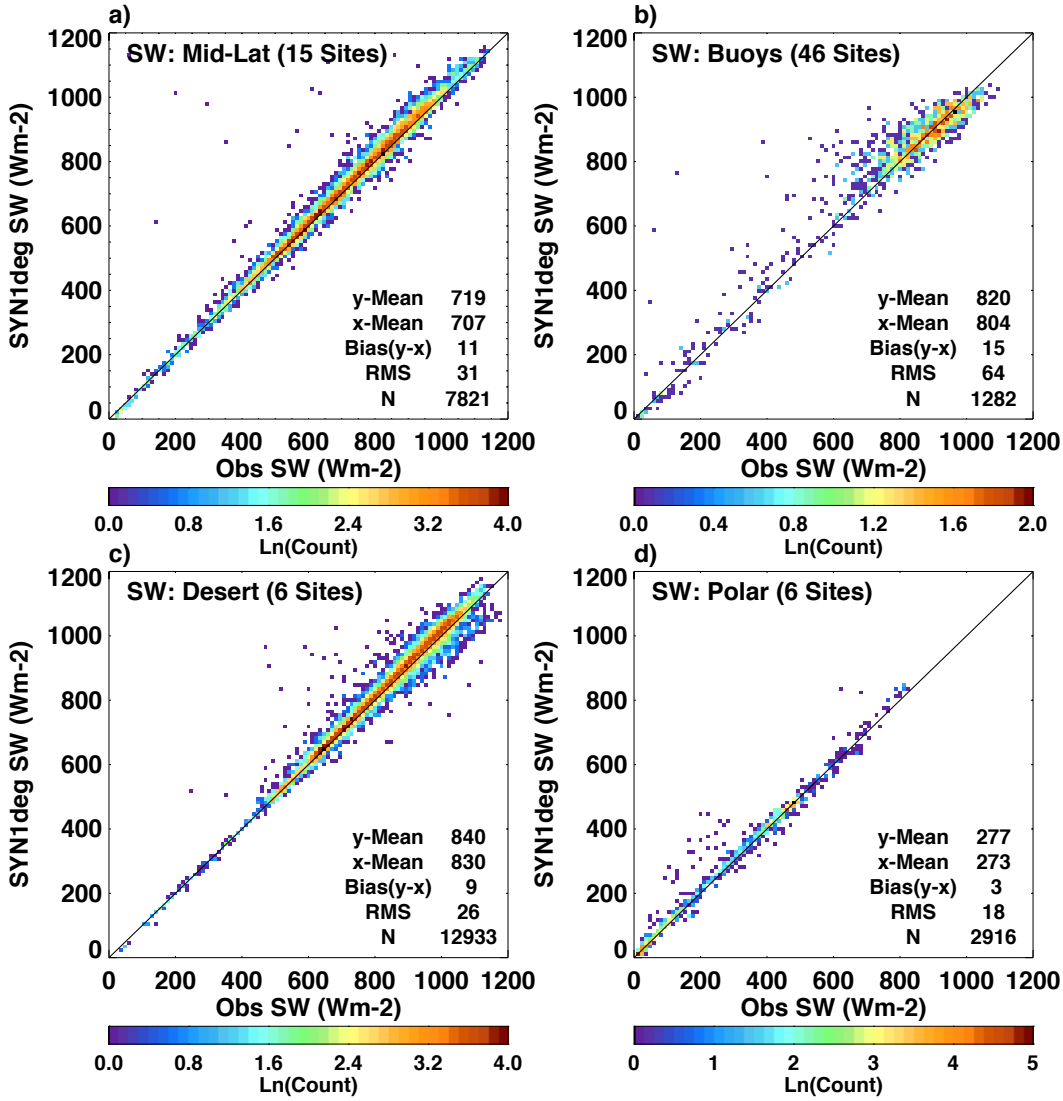

Figure 13. Comparisons of DSI at the surface from the SYN1deg Ed4.1 calculations (y-axis for all plots) and BSRN and buoy surface sites (x-axis all plots). Data are from Mar 2000 through Feb 2020 and only include hours when a 1° grid box is 100% clear sky according to SYN1deg cloud fraction.

Figure 13 shows hourly comparisons of computed clear-sky downward shortwave irradiance compared to observations for the groups of sites shown in **Fig. 11**. In general, calculated irradiance is larger than observed. We find that in every grouping, SYN1deg calculations tend to be too transmissive, overestimating DSI by between 3 Wm^{-2} (polar sites) and 15 Wm^{-2} (ocean buoys) with mid-latitude and desert sites each

458 overestimating DSI by ~10 Wm^{-2}. This points to the possibility that MATCH is weighted
459 too far towards scattering aerosols and too few absorbing aerosols.

460 Clear-sky scenes used for **Fig. 13** are those identified by MODIS and
461 geostationary satellites over the 1° grid box where the ground site is located. That is,
462 when satellites did not detect clouds over the one-hour period within the grid box, we
463 compared computed and observed hourly mean downward shortwave irradiances. DSI is
464 nominally measured by a shaded pyranometer combined with the direct insolation
465 measured by a pyrheliometer on a solar tracker. Though satellites may indicate clear,
466 clouds might have been present within the field-of-view of the pyranometer increasing
467 diffuse radiation. This would increase observed DSI, hence modeled irradiance would be
468 smaller. To verify, we used the ground-based cloud screening algorithm developed by
469 Long and Ackerman (Long et al. 2006) to further screen clouds. For the land groupings,
470 Table 5 shows bias (RMS) of the DSI where both satellite and surface based observed
471 cloud fraction equal 0.0. Though mean bias did not change significantly, the RMS in both
472 the Mid-Latitude and Desert sites was reduced by half due to the more stringent cloud
473 screening.

Table 5. Bias (RMS) of clear sky surface shortwave calculation compared to observation[1].
All in Wm^{-2}

Cloud Analysis	Mid Latitude	Desert	Polar
Satellite	11 (31)	9 (26)	3 (18)
Satellite And Surface	11 (16)	8 (15)	4 (19)

[1]Sample is based on 20 years of calculations when either satellite or satellite and surface cloud analysis indicates 0% cloud.

474

475 **4.2 Longwave Comparisons**

476 In this section we consider the implications of errors in AOD and aerosol type on

longwave LFLRT calculations as found in the SYN1deg product. **Figure 14** shows SYN1deg surface downward longwave irradiance (DLI) calculations compared to surface

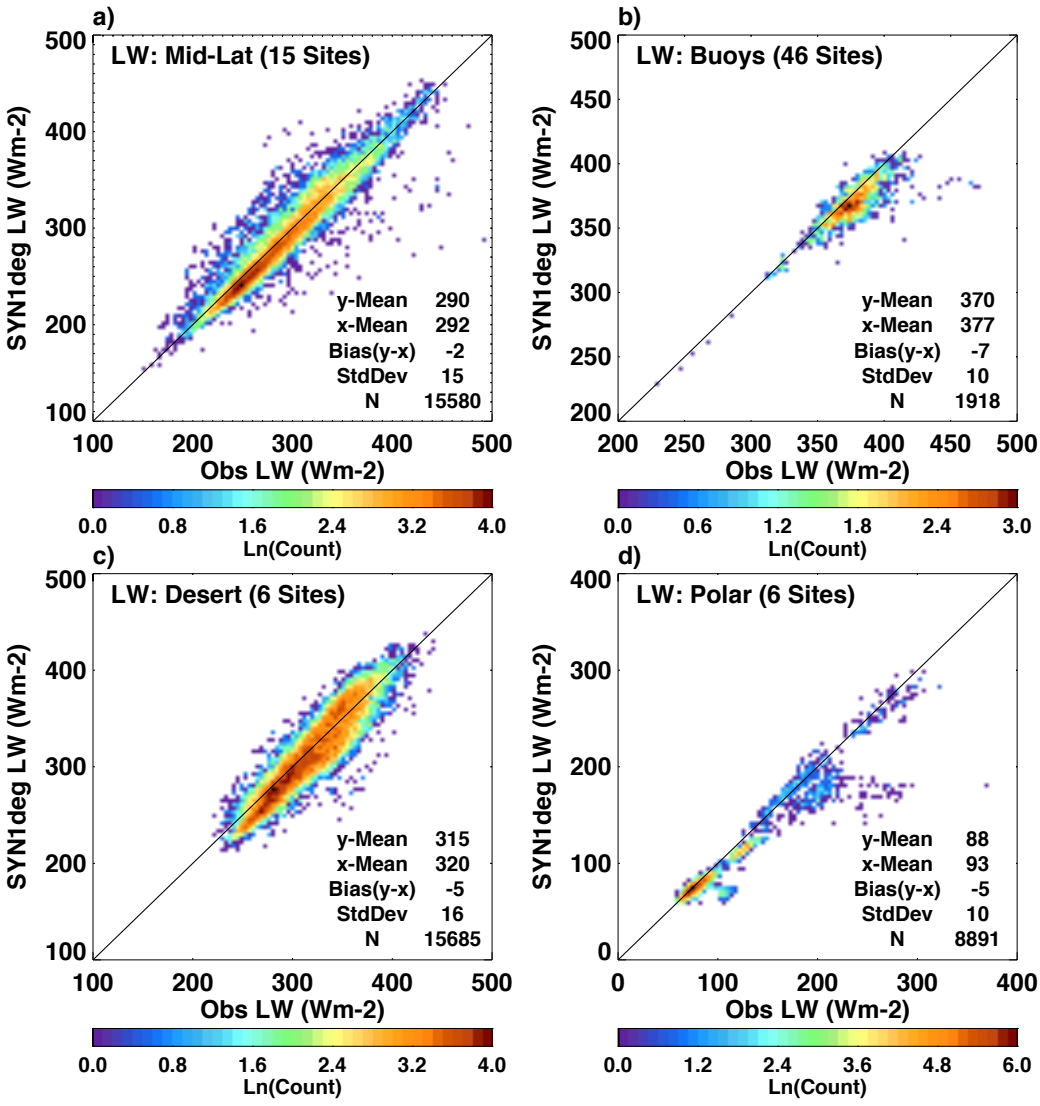

Figure 14. Comparisons of LW downward irradiance at the surface from the SYN1deg Ed4.1 calculations (y-axis for all plots) and BSRN and buoy surface sites (x-axis all plots). Data are from Mar 2000 through Feb 2020 and only include hours when a 1x1 grid box is 100% clear sky according to SYN1deg cloud fraction.

observations similar to those shown in **Fig. 13**. Except for the polar region, where DLI is very sensitive to near surface air temperature, the bias and standard deviations of the DLI

is smaller than the SW equivalents in terms of both Wm^{-2} and percentage of the mean observation. Depending on aerosol type, DLI is less sensitive to total AOD. For example, a doubling of AOD (0.2 to 0.4) for a continental type results in a DLI change of only 0.2 W m^{-2}. Table 6, however, shows the sensitivity of DLI (and DSI) to changes in dust particle size and shows that for LW, a change in aerosol type results in up to a 10 Wm^{-2} change in DLI.

Table 6. Effect of Dust Particle size on Surface Irradiance Calculations[1]

	Dust Particle Size (microns)		
	0.5	2.0	8.0
DLI	352 Wm^{-2}	359 Wm^{-2} (+2.0%)	362 Wm^{-2} (+2.8%)
DSI	1046 Wm^{-2}	1028 Wm^{-2} (-1.7%)	1020 Wm^{-2} (-2.5%)

[1]The radiative transfer code is run for a Mid-Latitude Summer atmosphere, open shrub surface albedo, aerosol scale height of 1.5km, clear sky, and cosine solar zenith angle of 1.0. Aerosol optical depth is fixed at 0.2 for all calculations.

DLI is thus more sensitive to aerosol type in certain regions of the globe where there is substantial dust. To see the potential impact on DLI **Figure 15** shows calculated LW downward radiative forcing (clear minus pristine calculations) at 57 AERONET sites across the 20 years of SYN1deg data under consideration. The Northwest Africa sites (where dust is found seasonally) are shown as red boxes where one clearly sees larger LW forcing at these sites. Given the importance of particle size to LW effect we check MATCH particle size against AERONET fine/coarse mode retrievals for several of the African AERONET sites. **Figure 16** plots canonical mean observations of fine and coarse mode AOD from three AERONET sites along with groupings of AOD species from the MATCH model output. To compare to AERONET fine mode observations we plot the sum of the MATCH AOD due to organic carbon (OC), black carbon (BC) and sulfate

(SO4). We compare the sum of MATCH AOD large dust particles (> 1um) along with sea salt (though sea salt is essentially zero over land) to the coarse mode AERONET optical depth. All AOD values are at 550nm.

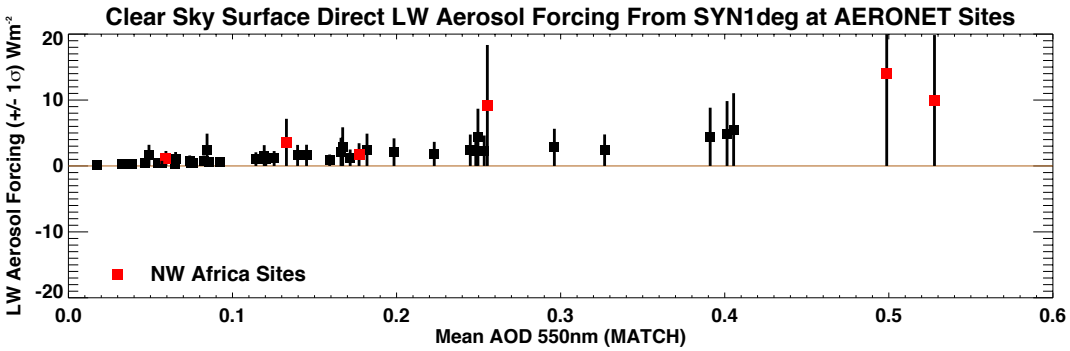

Figure 15. Clear sky direct radiative effect (clear minus pristine) in downward longwave irradiance averaged from 2000 through 2020 when AERONET observations are available. Boxes indicate average, vertical bar is +/- one standard deviation. Black boxes indicate all 57 AERONET sites and red boxes indicate Northwest Africa sites.

Figure 16 indicates that resultant fine/coarse mode comparisons are encouraging but the agreement is site dependent. In general MATCH is capturing seasonal changes in fine and coarse particles at these sites but the magnitude of the AODs is biased.

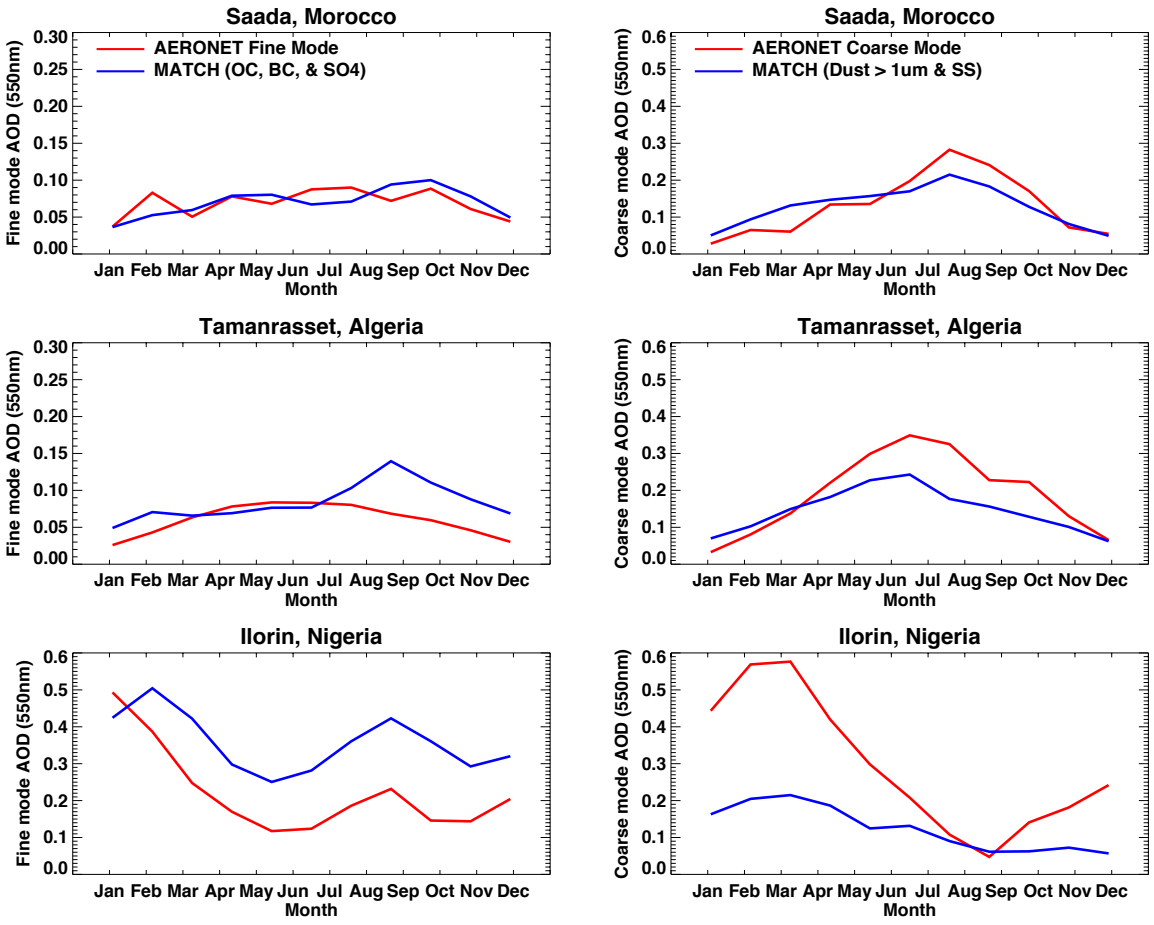

Figure 16. Canonical monthly means across 20 years (2000-2020) showing AERONET fine (left) and coarse (right) AOD at 550nm compared to MATCH constituents. MATCH values represent summations of organic, black carbon (OC, BC) and sulfate (SO4) for fine mode and large dust particles (> 1micron) plus sea salt for coarse mode comparisons.

510

511 **4.3 CERES TOA and EBAF-surface comparison**

512 CERES instruments observe TOA irradiances, which can be used to assess the

513 bias in computed irradiance. Global annual mean clear-sky TOA irradiances derived from

514 CERES observation averaged over 20 years from March 2000 through February 2020 are

515 53 Wm^{-2} for reflected shortwave irradiance and 268 Wm^{-2} for emitted longwave

516 irradiance. Corresponding computed reflected shortwave flux is 51 Wm^{-2} and emitted

517 longwave flux is 267 Wm^{-2}. Insight into the surface irradiance errors may be gained by

518 considering how surface irradiance is modified via the tuning algorithm to match TOA
519 irradiance in the CERES EBAF-surface product (Kato et al. 2018). After known biases
520 are taken out, the adjustment of temperature and specific humidity profiles, surface and
521 aerosol properties are derived based on their pre-assigned uncertainty and the difference
522 of computed and observed TOA shortwave and longwave irradiance using the Lagrange
523 multiplier approach. To match the computed shortwave and longwave fluxes, AOD is
524 increased from 0.136 to 0.156 (global annual mean values) and precipitable water is
525 decreased from 2.29 cm to 2.22 cm (global annual mean values). These adjustments
526 change the downward shortwave irradiance from 244 Wm^{-2} to 243 Wm^{-2}.
527 To analyze how the EBAF tuning process changes surface irradiance, AOD and
528 precipitable water, we computed the mean change separated by surface group shown in
529 **Fig 11**. Generally, AOD increases and precipitable water decreases to increase reflected
530 shortwave flux, which in turn decreases surface downward shortwave irradiance over
531 these regions (**Table 6**). For the midlatitude group, on average, AOD is increased by
532 0.02, precipitable water is decreased by 0.06 cm, and surface albedo is increased by 0.03.
533 These adjustments reduce the diurnally averaged downward shortwave irradiance at the
534 surface by 2 Wm^{-2}. We do not have exact matches of BSRN and AERONET surface sites
535 but Tables 3 and 4 show MATCH AODs have either no bias (north America and China
536 and southeast Asia) or slightly negatively biased by 0.01 (Europe). Therefore, increasing
537 MATCH AODs by 0.02 on average for the mid-latitude group seems justifiable.
538 However, decreasing 2 Wm^{-2} for the diurnally averaged downward shortwave is smaller
539 than the 11 Wm^{-2} bias shown in the top left plot of **Fig. 13**, although instantaneous
540 irradiances are used for **Fig. 13**. The positive bias found in the downward shortwave

541 irradiance for the North Africa group (**Fig 13c**) is not consistent with the positive bias of
542 aerosol optical depth shown in **Table 3** under clear-sky conditions.
543 The adjustment made to match TOA shortwave irradiance, in the EBAF product,
544 is within the uncertainty of MODIS-derived AOD of ±0.05 over land and ±0.03 over
545 ocean (Remer et al. 2008; Levy et al. 2010, 2013). However, these are an expected error
546 of instantaneous AOD retrieval derived from the comparison of AODs with AERONET.
547 Therefore, the bias averaged over ground sites and many years is expected to be much
548 smaller. Although, the 0.03 AOD adjustment over ocean might be the upper limit of the
549 uncertainty of MODIS AODs over ocean, 16 Wm^{-2} bias in the instantaneous downward
550 shortwave irradiance seems to be larger than the reduction by 2 Wm^{-2} in the diurnally
551 averaged downward shortwave irradiance.
552 While we cannot identify the cause of the discrepancy between AOD comparison
553 and downward shortwave irradiance comparison with surface observations, potential
554 issues are following. 1) Aerosol type and optical properties used in irradiance
555 computations, and 2) bias in downward shortwave irradiance measured by pyranometer,
556 especially diffuse irradiance at smaller solar zenith angles. Because of the temperature
557 gradient within pyranometer, the downward shortwave irradiance measured by a
558 pyranometer tends to be biased low under clear-sky condition (Haeffelin et al. 2001).
559 Note that a study by Ham et al. (2020) indicates that the bias of diurnally averaged
560 surface downward shortwave irradiance computed by a four-stream model should be
561 smaller than 1%.
562
563

Table 6: Radiative flux, aerosol optical depth (AOD), precipitable water, and surface albedo change to match observed top-of-atmosphere radiative fluxes

Site	Observed TOA upward shortwave irradiance (Wm-2)	Changes: Adjusted - Unadjusted				
		Clear-sky TOA upward shortwave irradiance (Wm-2)	Clear-sky surface downward shortwave irradiance (Wm-2)	Clear-sky AOD	Clear-sky precipitable water (cm)	Clear-sky surface albedo
Mid-Latitude	63.3	3.9	-2.0	0.02	-0.06	0.03
Desert	92.3	3.4	-1.7	0.02	-0.04	0.01
Polar	86.5	8.2	-0.2	0.01	-0.03	0.10
Buoys	42.0	1.6	-2.0	0.03	-0.12	0.00

5. Conclusions

We evaluated MATCH aerosol optical depth used to produce the CERES SYN1deg product. Aerosol optical depths derived from Terra and Aqua by the dark target and deep blue algorithms were merged to produce daily gridded AODs. Daily gridded AODs were used for assimilation by MATCH at local solar noon. As a consequence, monthly mean AODs under clear-sky conditions identified by MODIS closely agree with those derived from MODIS, although MATCH uses climatological aerosol sources. Because AODs are not screened by QAC, MATCH AODs are larger over convective regions (e.g. Amazon, central Africa, and south east Asia) for both clear-sky and all-sky conditions.

MATCH AODs under all-sky conditions are larger than those under clear-sky conditions. Time series of AERONET AODs indicate that AODs generally increase with cloud fraction, which is consistent with, primarily, water uptake by hygroscopic aerosols (Varnai et al, 2017). In addition, surface observations at the ARM SGP site suggest that a larger AODs and larger precipitable water under all-sky conditions than those under

clear-sky conditions. Aerosol optical depth biases from AERONET AODs are comparable to biases of MERRA2 AOD biases from AERONET AODs for both all-sky and clear-sky conditions. However, MERRA2, which uses AERONET AODs to train the algorithm, has better temporal correlation with AERONET AODs than MATCH AODs.

Once MATCH AODs are used for surface irradiance computations, downward shortwave irradiances are positively biased by 1% to 2% compared to those observed at surface sites. Top-of-atmosphere reflected clear-sky shortwave irradiances are negatively biased compared with those derived from CERES observations. Increasing AODs by ~0.02, and surface albedos by 0.03, and decreasing precipitable water by 0.06 cm over mid-latitude surface sites makes computed reflected TOA irradiances agree with those derived from CERES. These adjustments reduce downward shortwave irradiances at the surface by 2 Wm^{-2}. Decreasing MATCH AODs for the desert group is needed to match computed reflected shortwave irradiances at TOA with those derived from CERES. However, decreasing MATCH AODs is not consistent with generally larger MATCH AODs compared with AERONET.

Optical properties of aerosols (i.e. aerosol type) play a role in computing shortwave and longwave irradiance and changing and/or incorrect aerosol type can alter the downward irradiances. Aerosol types used in the computations rely on the mapping of MATCH types to those available in the radiative transfer model (Table 2). Biases in the fraction of each aerosol type and their optical properties can change TOA upward and surface downward shortwave irradiances without altering total AOD. A fuller evaluation of aerosol type is left for future study.

Acknowledgments

This work was funded by the NASA CERES project. The products and the validation could not have been accomplished without the help of the CERES TISA team. These data were obtained from the NASA Langley Research Center EOSDIS Distributed Active Archive Center. We also wish to acknowledge the hard work put in by the many dedicated scientists maintaining surface instrumentation in many diverse climates to obtain high quality observations of downwelling shortwave and longwave surface flux. Those groups are noted in Appendix A.

Appendix A. Surface Observation Sites Used for Validation

A great deal of data used in this study was collected by dedicated site scientists measuring critical climate variables around the world. The tables included in this appendix outline the sites, in situ measurements taken and their locations and dates of available data. Table A1 lists the locations of the AERONET sites, our source for observed aerosol optical depth which can be found on-line at: https://aeronet.gsfc.nasa.gov/new_web/index.html.

Table A1. AERONET Observation Sites

Region	Site	Location	Available Months
North Africa (5 Sites)	Saada, Morocco	31.6N, 8.2W	2004/07 - 2019/04
	Ouarzazate, Morocco	30.9N, 6.9W	2012/02 - 2015/06
	Dhaka, Morocco	23.7N, 15.9W	2002/02 - 2005/11
	Tamanrasset, Algeria	22.8N, 8.2E	2004/07 - 2019/04
	Cape Verde Island	16.7N, 22.9W	2000/03 - 2018/12
Central Africa (5 Sites)	Ilorin, Nigeria	8.5N, 4.7E	2000/03 - 2019/09
	Koforidua, Ghana	6.1N, 0.3W	2012/12 - 2019/04
	Lope, Gabon	0.2S, 11.6E	2014/04 - 2018/02
	Mbita, Kenya	0.4S, 34.2E	2006/03 - 2017/17
	Bujumbura, Burundi	3.4S, 29.4E	2013/12 - 2019/04
China, Korea (8 Sites)	Xinglong, China	40.4N, 117.6E	2006/02 - 2014/11
	Beijing, China	39.9N, 116.4E	2001/03 - 2019/03
	Anymon Isl, S Korea	36.5N, 126.3E	2000/03 - 2019/11
	Yonsei Univ, S Korea	37.6N, 126.9E	2011/03 - 2019/01
	Cuiying Mt, China	35.9N, 104.1E	2006/07 - 2013/05
	Nanjing, China	32.2N, 118.7E	2008/03 - 2010/04
	Taihu, China	31.4N, 120.2E	2005/09 - 2016/08
	XiangHe, China	39.7N, 116.9E	2001/03 - 2017/05
India, SE Asia (8 Sites)	Gandhi College, India	25.8N, 84.1E	2006/04 - 2019/11
	Luang Namtha, Laos	20.9N, 101.4E	2001/04 - 2019/02
	Omkoi, Thailand	17.8N, 98.4E	2003/02 - 2018/03
	Dhaka Univ, Bangledesh	23.7N, 90.3E	2012/06 - 2019/07
	Bhola, Bangledesh	22.2N, 90.7E	2013/04 - 2019/04
	Nghia Do, Vietnam	21.0N, 105.8E	2010/11 - 2019/09
	Pune, India	18.5N, 73.8E	2004/10 - 2019/06
	Hanimaadhoo, Maldives	6.7N, 73.2E	2004/11 - 2019/09

Table A1. AERONET Observation Sites (Continued)

Region	Site	Location	Available Months
Brazil (7 Sites)	Petrolina, Brazil	9.1S, 40.4W	2004/07 - 2016/11
	Abracos Hill, Brazil	10.7S, 62.4W	2000/03 - 2005/10
	Alta Floresta, Brazil	9.9S, 56.1W	2000/05 - 2019/02
	Belterra, Brazil	2.6S, 55.0W	2000/03 - 2005/04
	Ji Parana SE, Brazil	10.9S, 61.9W	2006/01 - 2017/10
	Manaus, Brazil	2.9S, 60.0W	2011/02 - 2019/05
	Rio Branco, Brazil	9.9S, 67.9W	2000/07 - 2017/10
Australia (6 Sites)	Jabiru, Australia	12.6S, 132.9E	2000/03 - 2019/09
	Lake Argyle, Australia	16.1S, 128.7E	2001/10 - 2019/09
	Canberra, Australia	35.3S, 149.1E	2003/01 - 2017/08
	Birdsville, Australia	25.9S, 139.3E	2005/08 - 2018/06
	Lucinda, Australia	18.5S, 146.4E	2009/10 - 2020/01
	Lake Lefroy, Australia	31.2S, 121.7E	2012/06 - 2019/12
North America (10 Sites)	Brats Lake, Canada	50.2N, 104.7W	2000/03 - 2013/02
	Sioux Falls, SD	43.7N, 96.6W	2001/06 - 2017/10
	Ames, IA	42.0N, 93.8W	2004/05 - 2019/03
	Boulder Tower	40.0N, 105W	2001/05 - 2016/07
	Bondville, IL	40.0N, 88.4W	2000/03 - 2017/10
	Brookhaven, NY.	40.8N, 72.9W	2002/09 - 2020/01
	Wallops Island, VA	37.9N, 75.5W	2003/03 - 2020/03
	ARM/SGP E13	36.6N, 97.5W	2000/03 - 2018/05
	Chesapeake Light Tower	36.9N, 75.7W	2000/03 - 2016/01
	Table Mountain, CO	40.1N, 105.2W	2008/11 - 2017/12
Europe (10 Sites)	Cabauw, Netherlands	51.9N, 4.9E	2003/04 - 2017/11
	Palaiseau, France	48.7N, 2.2E	2000/03 - 2020/10
	Torevere, Estonia	58.2N, 26.5E	2002/06 - 2019/07
	Kishinev, Moldova	47.0N, 28.8E	2000/03 - 2018/11
	Belsk, Poland	51.8N, 20.8E	2004/01 - 2016/08
	Kyiv, Ukraine	50.3N, 30.5E	2007/04 - 2018/12
	Hamburg, Germany	53.5N, 9.9E	2000/06 - 2018/06
	Munich Univ, Germany	48.1N, 11.6E	2001/11 - 2019/05
	Thessaloniki, Greece	40.6N, 22.1E	2003/06 - 2020/03
	Bucharest, Hungary	44.3N, 26.0E	2000/10 - 2019/03

Sources of surface observed downwelling irradiance are outlined in Tables A2 (land) and A3 (buoys). For land we utilize data from the Baseline Surface Radiation Network (BSRN) (Dreimel et al, 2018; Ohmura et al. (1998)), the US Dept. of Energy's Atmospheric Radiation Measurement (ARM) program and NOAA's SURFRAD network available from NOAA's Air Resources Laboratory/Surface Radiation Research Branch., Augustine et al. (2000). Buoy observations come from two sources through four separate projects. The Upper Ocean Processes group at Woods Hole Oceanographic Institute have maintained the Stratus, North Tropical

649 Atlantic Site (NTAS) and Hawaii Ocean Time Series (HOTS) buoys for more than a
650 decade providing valuable time series of radiation observations in climatically
651 important regions of the ocean. These data can be retrieved from:
652 http://uop.whoi.edu/index.html. We would also like to acknowledge the Project
653 Office of NOAA's Pacific Marine Environmental Labs (PMEL) where three groups of
654 buoy data were downloaded: In the Pacific, the Tropical Atmosphere
655 Ocean/Triangle Trans-Ocean Buoy Network (TAO/TRITON) (McPhaden, 2002) data,
656 from the tropical Atlantic Ocean, the Prediction and Research Moored Array in the
657 Tropical Atlantic (PIRATA) (Servain et al. 1998), and the Research Moored Array for
658 African - Asian - Australian Monsoon Analysis and Prediction (RAMA) (McPhaden et
659 al., 2009) in the Indian Ocean. Also downloaded from PMEL are the long-term buoy
660 observations PAPA and Kuroshio Current observatory sites.
661
662
663
664
665
666
667
668
669
670
671

Table A2. Surface Irradiance Validation Sites (Land)

Region	Site	Location	Source
Mid-Latitude (15 Sites)	Lindenberg, Germany	52.2N, 14.1E	BSRN
	Cabauw, Netherlands	51.9N, 4.9E	BSRN
	Fort Peck, MT	48.3N, 105.1W	BSRN
	Payerne, Switzerland	46.8N, 6.9E	BSRN
	Penn State, PA	40.7N, 77.9W	SURFRAD
	Beijing, China	39.9N, 116.3E	BSRN
	E13, Lamont, OK	36.6N, 97.5W	ARM
	Ches Light Tower, USA	36.9N, 75.7W	BSRN
	Tateno, Japan	36.1N, 140.1E	BSRN
	Goodwin Creek, MS	34.2N, 89.9W	SURFRAD
	De Aar, South Africa	30.6S, 24.0E	BSRN
	Lauder, New Zealand	45.0S, 169.7E	BSRN
	Florianapolis, Brazil	27.5S, 48.5W	BSRN
	Brasilia, Brazil	15.6S, 47.7W	BSRN
	Sao Martinho da Serra, Brazil	29.4S, 53.8W	BSRN
Desert (6 Sites)	Sede Boqer, Israel	30.8N, 34.7E	BSRN
	Saudi Solar Village	24.9N, 46.4E	BSRN
	Tamanrasset, Algeria	22.8N, 5.5E	BSRN
	Desert Rock, NV	36.6N, 116.1W	SURFRAD
	Alice Springs, Australia	23.7S, 133.8E	BSRN
	Gobabeb, Namibia	23.5S, 15.0E	BSRN
Polar (6 Sites)	Alert,Canada	82.5N, 62.4W	BSRN
	Tiksi, Russia	71.6N, 128.9E	BSRN
	Barrow, Alaska	71.3N, 156.7W	BSRN
	Syowa, Antarctica	69.0S, 39.5E	BSRN
	South Pole, Antarctica	90.0S, 0.5E	BSRN
	G. von Neumayer, Antarctica	-70.6S, 8.3W	BSRN

BSRN: Baseline Surface Radiation Network, http://bsrn.awi.de/
SURFRAD: NOAA- SURFace RADiation Program, http://www.esrl.noaa.gov/gmd/grad/surfrad/
ARM: US Dept of Energy, Atmospheric Radiation Measurement Program, http://www.arm.gov/

Table A3. Surface Observation Sites for Ocean Buoy Locations

Program Name	Data Source	Locations
Upper Ocean Processes Group (UOP) 3 Buoys	Woods Hole Oceanographic Institute	Stratus Buoy -20.2N, 85.0W
		North Tropical Atlantic Buoy 14.5N, 51.0W
		Hawaii Ocean Time Series Buoy 22.5N, 158W
PIRATA Buoys 14 Buoys	Pacific Marine Environmental Laboratory (PMEL)	East Atlantic Ocean
RAMA Buoys 10 Buoys	PMEL	Tropical Indian Ocean
TAO Array Buoys 17 Buoys	PMEL	E & W Tropical Pacific Ocean
Kuroshio Extension Observatory Buoy	PMEL	NW Pacific, 32.4N, 144.6E
PAPA Sub-Arctic Ocean Buoy	PMEL	NE Pacific, 50.1N, 144.8W

UOP: http://uop.whoi.edu/projects/projects.htm
PMEL: http://www.pmel.noaa.gov/tao/data_deliv/deliv.html

680 **References**

681 Augustine, J. A., DeLuisi, J. J., and Long, C. N.: SURFRAD – A national surface radiation
682 budget network for atmospheric research, Bull. of Amer. Met. Soc. 81, No. 10, pp.
683 2341-2358, 2000.
684 Barth, M. C., Rasch, P. J., Kiehl, J. T., Benkovitz, C. M., and Schwartz, S. E.: Sulfur
685 chemistry in the NCAR CCM: Description, evaluation, features and sensitivity to
686 aqueous chemistry, J. Geophys. Res., 106, 20 311–20 322, 2000.
687 Bauer, S. E. and Menon, S.: Aerosol direct, indirect, semidirect, and surface albedo
688 effects from sector contributions based on the IPCC AR5 emissions for
689 preindustrial and present-day conditions, J. Geophys. Res., 117, D01206,
690 doi:10.1029/2011JD016816, 2012.
691 Benkovitz, C. M., Scholtz, M. T., Pacyna, J., Tarrason, L., Dignon, J., Voldner, E. C., Spiro,
692 P. A., Logan, J. A., and Graedel, T. E.: Global gridded inventories of anthropogenic
693 emissions of sulfur and nitrogen, J. Geophys. Res.: Atmos. 101 (D22), 29,239–
694 29,253, 1996.
695 Blanchard, D. C. and Woodcock, A. H.: The production, concentration and vertical
696 distribution of the sea-salt aerosol, Ann. Of the NY Acad. Of Sci.,
697 doi:10.1111/j.1749-6632.1980.tb17130, 1980.
698 Boucher, O., Randall, D., Artaxo, P., Bretherton, C., Feingold, G., Forster, P., Kerminen,
699 V.-M., Kondo, Y., Liao, H., Lohmann, U., Rasch, P., Satheesh, S.K., Sherwood, S.,
700 Stevens, B. and Zhang, X. Y.: Clouds and Aerosols. In: Climate Change 2013: The
701 Physical Science Basis. Contribution of Working Group I to the Fifth Assessment
702 Report of the Intergovernmental Panel on Climate Change [Stocker, T.F., D. Qin,

G.-K. Plattner, M. Tignor, S.K. Allen, J. Boschung, A. Nauels, Y. Xia, V. Bex and P.M. Midgley (eds.)]. Chapter 7. Cambridge University Press, Cambridge, United Kingdom and New York, NY, U, 2013.

Colbo, K. and Weller, R. A.: Accuracy of the IMET sensor package in the subtropics. J. Atmos. Oceanic Technol., 26, 1867–1890, https://doi.org/10.1175/2009JTECHO667.1, 2009.

Collins, W. D., Rasch, P. J., Eaton, B. E., B. Khattatov, V., Lamarque, J-F. and Zender, C. S.: Simulating aerosols using a chemical transport model with assimilation of satellite aerosol retrievals: Methodology for INDOEX. J. Geophys. Res., 106 (D7), 7313–7336, 2001.

d' Almeida, G. A., P. Koepke and E. P. Shettle: Atmospheric Aerosols: Global Climatology and Radiative Characteristics. A. Deepak Publishing, 561 pp. 1991

Driemel, A., and Co-authors: Baseline Surface Radiation Network (BSRN): structure and data description (1992–2017), Earth Syst. Sci. Data, 10, 1491-1501, doi:10.5194/essd-10-1491-2018. 2018

Emmons, L. K., and co-authors: Description and evaluation of the Model for Ozone and Related chemical Tracers, version 4 (MOZART-4), Geosci. Model Dev., **3**, 43–67. www.geosci-model-dev.net/3/43/2010/, 2010.

Fu, Q. and Liou, K-N.: Parameterization of the radiative properties of cirrus clouds, J. Atmos. Sci., 50, 2008–2025, 1993.

Fu, Q., Lesins, G., Higgins, J., Charlock, T., Chylek, P. and Michalsky, J.: Broadband water vapor absorption of solar radiation tested using ARM data. Geophys. Res. Let., 25, 1169–1172, 1998.

726 Ginoux, P., Chin, M., Tegen, I., Prospero, J. M., Holben, B., Dubovik, O. and Lin, S-J.:
727 Sources and distributions of dust aerosols simulated with the GOCART model J. of
728 Geophys. Res.: Atmos., 106, 20255-20273, doi.org/10.1029/2000JD000053, 2001.
729 Haeffelin, M., Kato, S., Smith, A. M., Rutledge, C. K., Charlock T. P. and Mahan, J. R.:
730 Determination of the thermal offset of the Eppley precision spectral pyranometer,
731 Appl. Opt. 40, 472-484, 2001.
732 Ham, S., Kato, S. and Rose, F. G.: Examining biases in diurnally-integrated shortwave
733 irradiances due to two- and four-stream approximations in cloudy atmosphere. J.
734 Atmos. Sci., 77(2), 551–581. doi: 10.1175/JAS-D-19-0215.1, 2020.
735 Hess, M., Koepke, P. and Schult, I.: Optical Properties of Aerosols and Clouds: The
736 software package OPAC. Bull. Amer. Meteor. Soc., 79, 831-844.
737 https://doi.org/10.1175/1520-0477(1998)079<0831:OPOAAC>2.0.CO;2,1998.
738 Holben B.N., Eck, T. F., Slutsker, I., Tanre, D., Buis, J. P., Setzer, A., Vermote, E.,
739 Reagan, J. A., Kaufman, Y., Nakajima, T., Lavenu, F., Jankowiak, I. and Smirnov,
740 A.: AERONET - A federated instrument network and data archive for aerosol
741 characterization, Rem. Sens. Environ., 66, 1-16, 1998
742 Hsu, N. C., Tsay, S-C, King, M. D. and Herman, J. R.: Deep Blue Retrievals of Asian
743 Aerosol Properties During ACE-Asia, IEEE Trans. On Geosci. and Rem. Sens.,
744 44(11), 2006.
745 Huneeus, N., and co-authors: Global dust model intercomparison in AeroCom phase I,
746 Atmos. Chem. Phys., 11, 7781–7816. www.atmos-chem-phys.net/11/7781/2011/
747 doi:10.5194/acp-11-7781-2011, 2011.

748 Kato, S., Loeb, N. G., Rose, F. G., Doelling, D. R., Rutan, D. A., Caldwell, T. E., Yu L.
749 and Weller, R. A.: Surface irradiances consistent with CERES-derived top-of-
750 atmosphere shortwave and longwave irradiances. J. of Clim Dyn. doi: 10.1175/JCLI-
751 D-12-00436, 2013.
752 Kato, S., Rose, F. G., Rutan, D. A., Thorsen, T. J., Loeb, N. G., Doelling, D. R., Huang,
753 X., Smith, W. L., Su, W. and Ham, S-H.: Surface Irradiances of Edition 4.0 Clouds
754 and the Earth's Radiant Energy System (CERES) Energy Balanced and Filled
755 (EBAF) Data Product. J. of Clim Dyn. doi: 10.1175/JCLI-D-17-0523.1, 2018.
756 Kaufman, Y. and co-authors: A critical examination of the residual cloud contamination
757 and diurnal sampling effects on MODIS estimates of aerosol over ocean, IEEE Trans.
758 Geosci. Rem. Sens. 43, DOI: 10.1109/TGRS.2005.858430, 2005.
759 Kinne, S. and co-authors: An AeroCom initial assessment – optical properties in aerosol
760 component modules of global models. Atmos. Chem. Phys., 6, 1815–1834.
761 www.atmos-chem-phys.net/6/1815/2006/, 2006.
762 Koch, D., and co-authors: Evaluation of black carbon estimations in global aerosol
763 models. Atmos. Chem. Phys., 9, 9001–9026. www.atmos-chem-
764 phys.net/9/9001/2009/, 2009.
765 L'Ecuyer T. S., Beaudoing, H. K., Rodell, M., Olson, W., Lin, B., Kato, S., Clayson, C.
766 A., Wood, E., Sheffield, J., Adler, R., Huffman, G., Bosilovich, M., Gu, G.,
767 Robertson, F., Houser, P. R., Chambers, D., Famiglietti, J. S., Fetzer, E., Liu, W. T.,
768 Gao, X., Schlosser, C. A., Clark, E., Lettenmaier, D. P. and Hilburn, K.: The
769 observed state of the energy budget in the early twenty-first century. J Clim
770 28(21):8319–8346. https://doi.org/10.1175/Jcli-D-14-00556.1, 2015.

771 Levy, R. C., Remer, L. A., Kleidman, R. G. , Mattoo, S., Ichoku, C., Kahn R. and Eck, T.
772 F.: Global evaluation of the collection 5 MODIS dark-target aerosol products over
773 land. Atmos. Chem and Phys., 10, 103999-10420. https://doi.org/10.5194/acp-10-
774 10399-2010, 2010.
775 Levy, R. C., Mattoo, S., Munchak, L. A., Remer, L. A., Sayer, A. M., Patadia, F. and
776 Hsu, N. C.: The Collection 6 MODIS aerosol products over land and ocean. Atmos.
777 Meas. Tech., 6, 2989-3034, 10.5194/amt-6-2989-2013, 2013.
778 Liousse, C., Penner, J. E., Chuang, C., Walton, J. J., Eddleman, H. and Cachier, H.: A
779 global three-dimensional model study of carbonaceous aerosols, J. Geophys. Res. A.,
780 101(D14), 19 411– 19 432, 1996.
781 Loeb, N. G., Kato, S., Loukachine, K. and Smith, N. M.: Angular Distribution Models for
782 Top-of-Atmosphere Radiative Flux Estimation from the Clouds and the Earth's
783 Radiant Energy System Instrument on the Terra Satellite. Part I: Methodology, J.
784 Atmos. Oceanic Technol, 22, 338-351, 2005.
785 Loeb, N. G. and Su, W.: Direct Aerosol Radiative Forcing Uncertainty Based on a
786 Radiative Perturbation Analysis. J. Climate, 23(19), 5288-5293. doi:
787 10.1175/2010JCLI3543.1, 2010.
788 Loeb, N. G., Doelling, D. R., Wang, H., Su, W., Nguyen, C., Corbett, J. G., Liang, L., Mitrescu,
789 C., Rose, F. G. and Kato, S.: Clouds and the Earth's Radiant Energy System (CERES)
790 Energy Balanced and Filled (EBAF) top-of-atmosphere (TOA) Edition-4.0 data
791 product. J. Climate, 31, 895–918, https://doi.org/10.1175/JCLI-D-17-0208.1,
792 2018.

Loeb, N. G., Rose, F. G., Kato, S., Rutan, D. A., Su, W., Wang, H., Doelling, D. R., Smith, W. L. and Gettelman, A.: Toward a Consistent Definition between Satellite and Model Clear-Sky Radiative Fluxes, J. Clim. DOI: 10.1175/JCLI-D-19-0381.1, 2020.

Long, C. N., Ackerman, T. P., Gaustad, K. L. and Cole, J. N. S.: Estimation of fractional sky cover from broadband shortwave radiometer measurements, J. Geophys. Res.,111, D11204, doi:10.1029/2005JD006475, 2006.

Martins, J. V., D. Tanre, D., Remer, L., Kaufman, Y., Mattoo, S. and Levy, R.: MODIS cloud screening for remote sensing of aerosols over oceans using spatial variability, Geophys. Res. Lett., 29, 1619, DOI:10.1029/2001GL013252, 2002.

Marshak, A., Ackerman, A., da Silva, A. M., Eck, T., Holben, B., Kahn, R., Kleidman, R., Knobelspiesse, K., Levy, R., Lyapustin, A., Oreopoulos, L, Remer, L., Torres, O., Várnai, T., Wen, G., and Yorks, J.: Aerosol properties in cloudy environments from remote sensing observations, Bul. Amer. Met. Soc., 102, E2177–E2197, https://doi.org/10.1175/BAMS-D-20-0225.1, 2021.

McPhaden, M. J.: TAO/TRITON tracks Pacific Ocean warming in early 2002. CLIVAR Exchanges, No. 24, International CLIVAR Project Office, Southampton, United Kingdom, 7–9, 2002.

#——, and Coauthors: RAMA: The Research Moored Array for African–Asian–Australian Monsoon Analysis and Pre- diction. Bull. Amer. Meteor. Soc., 90, 459–480, doi:10.1175/ 2008BAMS2608.1, 2009.

Michalsky, J. J., Gueymard, C., Kiedron, P., McArthur, L. J. B., Philipona, R. and Stoffel, T.: A proposed working standard for the measurement of diffuse horizontal

shortwave irradiance. J. of Geophys. Res. A., 112(D16), https://doi.org/10.1029/2007JD008651, 2007.

Minnis, P., Sun-Mack, S., Chen, Y., Chang, F., Yost, C. R., Smith, W. L., Heck, P. W., Arduini, R. F., Bedka, S. T., Yi, Y., Hong, G., Jin, Z., Painemal, D., Palikonda, R., Scarino, B. R., Spangenberg, D. A., Smith, R. A., Trepte, Q. Z., Yang, P. and Xie, Y.: CERES MODIS Cloud Product Retrievals for Edition 4–Part I: Algorithm Changes. IEEE Transactions on Geoscience and Remote Sensing, 1-37. doi: 10.1109/TGRS.2020.3008866, 2020.

Ohmura A., Dutton, E., Forgan, B., Frohlich, C., Gilgen, H., Hegne, H., Heimo, A., Konig-Langlo, G., McArthur, B., Muller, G., Philipona, R., Whitlock, C., Dehne, K. and Wild, M.: Baseline Surface Radiation Network (BSRN/WCRP): New precision radiometry for climate change research. Bull. Amer. Meteor. Soc., 79, No. 10, 2115-2136, 1998.

Randles, C. A., Da Silva, A. M., Buchard, V., Colarco, P. R., Darmenov, A., Govindaraju, R., Smirnov, A., Holben, A., Ferrare, R., Hair, J., Shinozuka, Y. and Flynn, C. J.: The MERRA-2 aerosol reanalysis, 1980 onward. Part I: System description and data assimilation evaluation, J. Clim. 30(17), http://dx.doi.org/10.1175/ JCLI-D-16-0609.s1, 2017.

Rasch, P. J., Mahowald, N. M. and Eaton, B. E.: Representations of transport, convection, and the hydrologic cycle in chemical transport models: Implications for the modeling of short-lived and soluble species. J. of Geo. Res., 102, 127-138, 1997.

Rasch, P. J., Collins, W. D. and Eaton, B. E.: Understanding the Indian Ocean

839 Experiment (INDOEX) aerosol distributions with an aerosol assimilation. J. of
840 Geo. Res., 106, 7337-7355, 2001.
841 Remer, L. A., and Co-authors: The MODIS aerosol algorithm, products, and validation. J.
842 Atmos. Sci., 62, 947–973, 2005.
843 Remer, L. A., Kleidman, R. G., Levy, R. C., Kaufman, Y. J., Tanre, D., Mattoo, S.,
844 Vanderlei Martins, J., Ichoku, C., Koren, I., Yu, H. and Holben, B. N.: Global aerosol
845 climatology from the MODIS satellite sensors. J. Geophys. Res.: A. 113(D14),
846 https://doi.org/10.1029/2007JD009661, 2008.
847 Rose, F. G, Rutan, D. A., Charlock, T., Smith, G. L. and Kato, S.: An Algorithm for the
848 Constraining of Radiative Transfer Calculations to CERES-Observed Broadband
849 Top-of-Atmosphere Irradiance. J. Atmos. and Ocean. Tech. 30, 1091-1106. DOI:
850 10.1175/JTECH-D-12-00058.1, 2013.
851 Rutan, D., Rose, F., Roman, M., Manalo-Smith, N., Schaaf, C. and Charlock, T.:
852 Development and assessment of broadband surface albedo from Clouds and the
853 Earth's Radiant Energy System clouds and radiation swath data product. J. Geophys.
854 Res., 114, D08125. doi:10.1029/2008JD010669, 2009.
855 Rutan, D., Kato, S., Doelling, D. R., Rose, F. G., Nguyen, L. T. and Caldwell, T.: CERES
856 Synoptic Product: Methodology and Validation of Surface Radiant Flux. J. Atmos.
857 And Ocean. Tech., 32, doi:10.1175/JTECH-D-14-00165.1, 2015.
858 Servain, J., Busalacchi, A. J., McPhaden, M. J., Moura, A. D., Reverdin, G., Vianna, M.
859 and Zebiak, S. E.: A Pilot Research Moored Array in the Tropical Atlantic
860 (PIRATA). Bull. Amer. Meteor. Soc., 79, 2019–2031, doi:10.1175/ 1520-
861 0477(1998)079,2019:APRMAI.2.0.CO;2. 1998

862 Sinyuk, A., Torres, O. and Dubovik, O.: Combined use of satellite and surface
863 observations to infer the imaginary part of refractive index of Saharan dust.
864 Geophysical Research Letters, 30(2), 1081. https://doi.org/10.1029/2002GL016189,
865 2003.
866 Smirnov, A., Holben, B. N., Eck, T. F., Dubovik, O. and Slutsker, I.: Cloud-screening
867 and quality control algorithms for the AERONET database. Rem. Sens. Env. 73, 337-
868 349, 2000.
869 Soden, B. and Chung, E-S.: The Large-Scale Dynamical Response of Clouds to Aerosol
870 Forcing. J. of Climate, 30, 8783-8794. doi: https://doi.org/10.1175/JCLI-D-17-
871 0050.1, 2017.
872 Stephens, G. L., Slingo, J. M., Rignot, E., Reager, J. T., Hakuba, M. Z., Durack, P. J.,
873 Worden, J. and Rocca, R.: Earth's water reservoirs in a changing climate. Proc. R.
874 Soc. A 476: 20190458. http://dx.doi.org/10.1098/rspa.2019.0458, 2020.
875 Su, W., Schuster, G. L., Loeb, N. G., Rogers, R. R., Ferrare, R. A., Hostetler, C. A., Hair,
876 J. W., and Obland, M. D.: Aerosol and cloud interaction observed from high spectral
877 resolution lidar data. J. of Geophys. Res.: Atmos., 113(D24), D24202.
878 Doi:10.1029/2008JD010588, 2008.
879 Su, W., Corbett, J., Eitzen, Z. and Liang, L.: Next-generation angular distribution models
880 for top-of-atmosphere radiative flux calculation from CERES instruments:
881 methodology. Atmos. Meas. Tech., 8(2), 611-632. doi: 10.5194/amt-8-611-2015,
882 2015.

883 Su, W., Corbett, J., Eitzen, Z. and Liang, L.: Next-generation angular distribution models
884 for top-of-atmosphere radiative flux calculation from CERES instruments: validation.
885 Atmos. Meas. Tech., 8(8), 3297-3313. doi: 10.5194/amt-8-3297-2015, 2015.
886 Su, W., G. L. Schuster, N. G. Loeb, R. R. Rogers, R. A. Ferrare, C. A. Hostetler, J. W.
887 Hair, M. D. Obland, 2008: Aerosol and cloud interaction observed from high spectral
888 resolution lidar data. J. of Geophy. Res,: Atmos., 113(D24), D24202.
889 Doi:10.1029/2008JD010588.
890 Textor, C. and Co-authors: Analysis and quantification of the diversities of aerosol
891 life cycles within AeroCom, Atmos. Chem. Phys., 6, 1777-1813. www.atmos-
892 chem-phys.net/6/1777/2006/, 2006.
893 Textor, C., and Co-authors: The effect of harmonized emissions on aerosol
894 properties in global models – an AeroCom experiment. Atmos. Chem. Phys., 7,
895 4489–4501. www.atmos-chem-phys.net/7/4489/2007/, 2007.
896 Varnai, T., Marshak, A. and Eck, T. F.: Observation-based study on aerosol optical depth
897 and particle size in partly cloudy regions. J. Geophys. Res: A. 122, 10,013–10,024,
898 https://doi.org/10.1002/2017JD027028, 2017.
899 Wen, G., Marshak, A., Cahalan, R. F., Remer, L. A. and Kleidman, R. G.: 3-D aerosol-
900 cloud radiative interaction observed in collocated MODIS and ASTER images of
901 cumulus cloud fields, J. Geophys. Res., 112, D13204, doi:10.1029/2006JD008267,
902 2007.
903 Wielicki, B. A., Barkstrom, B. R., Harrison, E. F., Lee, R. B. III, Smith, G. L. and Cooper, J.
904 E.: Clouds and the Earth's Radiant Energy System (CERES): An Earth Observing
905 System Experiment. Bull. Amer. Meteor. Soc., 77, 853-868, 1996.

906 Zender, C. S., Huishen, B. and Newman, D.: Mineral Dust Entrainment and Deposition
907 (DEAD) model: Description and 1990s dust climatology. J. Geophys. Res., 108,
908 doi:10.1029/2002JD002775, 2003.